

PLA2G15 is a BMP hydrolase and its targeting ameliorates lysosomal disease

<https://doi.org/10.1038/s41586-025-08942-y>

Received: 17 May 2024

Accepted: 25 March 2025

Published online: 7 May 2025

Open access

 Check for updates

Kwamina Nyame^{1,2,3,4,10}, Jian Xiong^{1,2,3,10}, Hisham N. Alsohybe^{1,2,3}, Arthur P. H. de Jong⁵, Isabelle V. Peña^{1,2,3}, Ricardo de Miguel⁶, Thijn R. Brummelkamp^{5,7}, Guido Hartmann⁵, Sebastian M. B. Nijman⁵, Matthijs Raaben⁵, Judith A. Simcox⁸, Vincent A. Blomen⁵ & Monther Abu-Remaileh^{1,2,3,9}✉

Lysosomes catabolize lipids and other biological molecules, maintaining cellular and organismal homeostasis. Bis(monoacylglycero)phosphate (BMP), a major lipid constituent of intralysosomal vesicles, stimulates lipid-degrading enzymes and is altered in various human conditions, including neurodegenerative diseases^{1,2}. Although lysosomal BMP synthase was recently discovered³, the enzymes mediating BMP turnover remain elusive. Here we show that lysosomal phospholipase PLA2G15 is a physiological BMP hydrolase. We further demonstrate that the resistance of BMP to lysosomal hydrolysis arises from its unique sn2, sn2' esterification position and stereochemistry, as neither feature alone confers resistance. Purified PLA2G15 catabolizes most BMP species derived from cell and tissue lysosomes. Furthermore, PLA2G15 efficiently hydrolyses synthesized BMP stereoisomers with primary esters, challenging the long-held thought that BMP stereochemistry alone ensures resistance to acid phospholipases. Conversely, BMP with secondary esters and *S,S* stereoconfiguration is stable in vitro and requires acyl migration for hydrolysis in lysosomes. Consistent with our biochemical data, PLA2G15-deficient cells and tissues accumulate several BMP species, a phenotype reversible by supplementing wild-type PLA2G15 but not its inactive mutant. Targeting PLA2G15 reduces the cholesterol accumulation in fibroblasts of patients with Niemann–Pick disease type C1 and significantly ameliorates disease pathologies in Niemann–Pick disease type C1-deficient mice, leading to an extended lifespan. Our findings established the rules governing BMP stability in lysosomes and identified PLA2G15 as a lysosomal BMP hydrolase and a potential target for therapeutic intervention in neurodegenerative diseases.

Lysosomes are vital for cellular waste removal, nutrient recycling and maintaining homeostasis, particularly by breaking down complex lipids using hydrolytic enzymes. Lipid degradation within lysosomes is facilitated by intralysosomal vesicles rich in a unique lipid called bis(monoacylglycero)phosphate (BMP)¹. BMP significantly enhances lysosomal lipid metabolism, and its imbalance is a hallmark of various lysosome-associated diseases, including age-related neurodegeneration, viral infection, cancer and atherosclerotic cardiovascular disease^{1–3}.

Although we recently identified the lysosomal BMP synthase³, which was then validated as the sole lysosomal BMP synthase in cells by another group that also identified potential circulating machineries that might make BMP⁴, many questions about BMP degradation remain. BMP is a structural isomer of phosphatidylglycerol with symmetrical acyl chain positions on the two glycerol moieties and a unique *S,S* stereoconfiguration^{1,2} (Fig. 1a). Partial deacylation of these phospholipids

generates one fatty acid and lysophosphatidylglycerol (LPG) (Fig. 1b), whereas its complete deacylation releases two fatty acids and glycerophosphorylglycerol (GPG)^{5–7} (Fig. 1c). BMP is stable in the lysosomal environment. However, the rules that govern BMP catabolism remain unclear. Some reports speculate that its unique stereochemistry may confer resistance to its degradation by lysosomal hydrolases, a necessity for its proposed function in stimulating lipid degradation in the lysosome⁸, whereas others indicate that BMP is susceptible to enzyme-mediated hydrolysis^{5,6,9–13}. Because of its therapeutic potential, understanding BMP turnover and uncovering its physiological hydrolases in the lysosome are of great interest. Here we show that the unique sn2, sn2' position of the acyl chains of BMP is required to protect *S,S* BMPs from lysosomal hydrolysis by the abundant lysosomal phospholipase A2 (PLA2G15), which we establish as a BMP hydrolase in addition to its role as a general acid phospholipase B. In a parallel genetic screening effort, we identified PLA2G15 as a modifier of cholesterol staining and

¹Department of Chemical Engineering, Stanford University, Stanford, CA, USA. ²Department of Genetics, Stanford University, Stanford, CA, USA. ³Institute for Chemistry, Engineering and Medicine for Human Health (Sarafan ChEM-H), Stanford University, Stanford, CA, USA. ⁴Department of Biochemistry, Stanford University, Stanford, CA, USA. ⁵Scenic Biotech, Science Park 301, Amsterdam, The Netherlands. ⁶Pathology Department, AnaPath Services GmbH, Liestal, Switzerland. ⁷Oncode Institute, Division of Biochemistry, The Netherlands Cancer Institute, Amsterdam, The Netherlands. ⁸Howard Hughes Medical Institute, Department of Biochemistry, University of Wisconsin–Madison, Madison, WI, USA. ⁹The Phil & Penny Knight Initiative for Brain Resilience at the Wu Tsai Neurosciences Institute, Stanford University, Stanford, CA, USA. ¹⁰These authors contributed equally: Kwamina Nyame, Jian Xiong. ✉e-mail: monther@stanford.edu

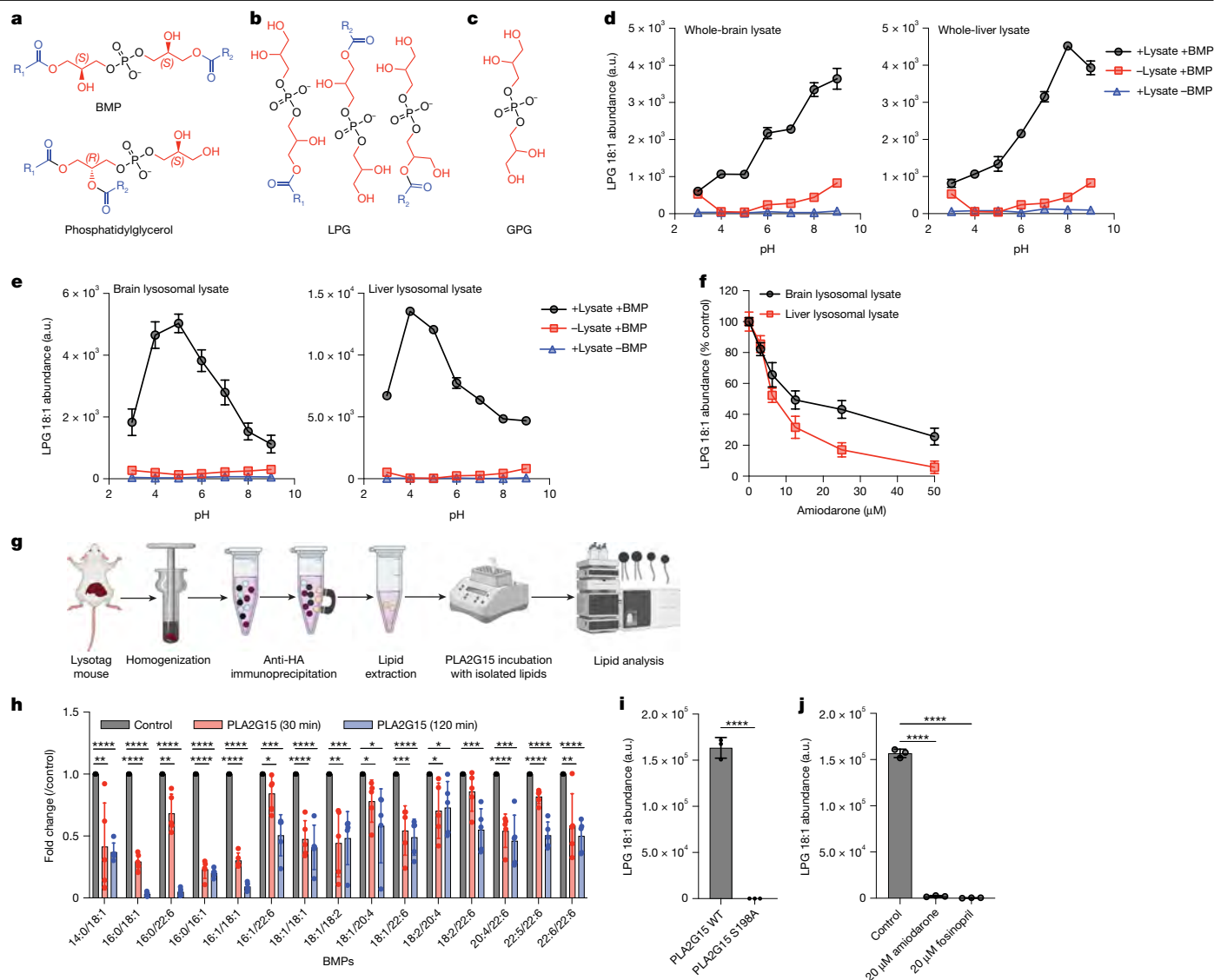


Fig. 1 | PLA2G15 hydrolyses BMP lipids. **a–c**, Chemical structures of BMP (top) and phosphatidylglycerol (bottom) (**a**) and their degradation intermediates LPG (all possible structures) (**b**) and GPG (**c**). Red represents two glycerol groups, and blue represents the acyl chains. **d**, BMP hydrolysis activity in the brain (left) and liver (right) lysates. The hydrolysis of 3,3′-18:1-S₂BMP (1 μM) in buffers with pH range between 3.0 and 9.0 (Methods). Controls had similar reaction buffers, except with no lysate or BMP. Data are presented as mean ± s.d. of three biological replicates. **e**, Lysosomal lysates hydrolyse BMP with an acidic optimum. As in **d** but using brain lysosomal lysate (left) and liver lysosomal lysate (right). Data are presented as mean ± s.d. of *n* = 3. **f**, As in **d** but using brain and liver lysosomal lysates and in increasing concentration of amiodarone under acidic conditions (pH 5.0). Data are presented as mean ± s.d. of three biological replicates. **g**, PLA2G15 hydrolysed BMPs isolated from mouse

liver lysosomes. **g**, Depiction of experimental design. **h**, Fold changes in the abundance of measured BMPs, and each time point was compared to the control. Data are presented as mean ± s.d. of five biological replicates. **P* < 0.05; ***P* < 0.01; ****P* < 0.001; *****P* < 0.0001 by two-tailed unpaired *t*-tests for each BMP. **i**, Hydrolysis of 1 μM 3,3′-18:1-S₂BMP by 100 nM recombinant wild-type PLA2G15 and S198A mutant under acidic conditions for 30-s reaction time. Data are presented as mean ± s.d. of three independent replicates. *****P* = 0.000014 by two-tailed unpaired *t*-test. **j**, As in **i** using wild-type PLA2G15 in the presence of 20 μM amiodarone and foscipril compared with the no inhibitor control. Data are presented as mean ± s.d. of three independent replicates. *****P* < 0.0001 by two-tailed unpaired *t*-tests. a.u., arbitrary units; WT, wild type. Panel **g** was created using BioRender (<https://biorender.com>).

showed that knockdown of PLA2G15 reduced cholesterol accumulation in the fibroblasts of patients with Niemann–Pick disease type C1 (NPC1). In addition, PLA2G15 inactivation in mice with NPC1 increased their lifespan and reduced the expression of key disease biomarkers. Thus, targeting PLA2G15 boosts levels of BMP and has therapeutic potential in NPC and possibly other lysosomal storage diseases.

PLA2G15 hydrolyses BMP lipids

To test whether BMP lipids are susceptible to phospholipase A (PLA)-mediated hydrolysis, we first incubated brain and liver lysates

with commercially available BMP with the physiologically relevant stereoconfiguration (S₂BMP)¹ and monitored the release of the LPG intermediate (Fig. 1d). Consistent with a previous report⁶, we observed a BMP hydrolase activity under both acidic and alkaline conditions, with relatively higher activity at neutral and mildly alkaline pH (Fig. 1d), probably because of the abundance of extralysosomal PLA in the lysate with minimal lysosomal protein contribution¹⁴. Although these results indicate that BMP is not inherently resistant to PLA, it can be protected by residing in the lysosome^{15,16}. To test whether lysosomal PLA can degrade BMP lipids under acidic pH conditions, we purified lysosomes from both tissues^{7,17}. Indeed, lysosomal lysates efficiently

hydrolysed BMP with an optimum pH of 4–5, reminiscent of that of the acid PLA⁷ (Fig. 1e). This activity was diminished by amiodarone, a non-specific inhibitor of lysosomal PLA^{18,19} (Fig. 1f). These data indicate that BMP lipids are vulnerable to degradation by lysosomal phospholipases^{5,9–11}, indicating that their unique stereoconfiguration alone may not be sufficient to ensure their stability within the lysosome.

PLA2G15 is the major lysosomal phospholipase^{12,20,21}, and we recently established its function as phospholipase B capable of catalysing the complete hydrolysis of phospholipids with high efficiency⁷. Given our results, we investigated whether PLA2G15 can degrade BMP lipids. To this end, we incubated lysosomal lipid extracts isolated from LysoTag mouse tissues^{7,17} with purified PLA2G15 (Extended Data Fig. 1a–c) and monitored the abundance of glycerophospholipids, with a focus on phosphatidylglycerol, the structural isomer of BMP (Fig. 1g). Consistent with its function, the abundance of most measured glycerophospholipids was significantly decreased (Extended Data Fig. 2a), with a concomitant increase in lysophospholipid intermediates (Extended Data Fig. 2b). Most BMP lipid species were also significantly hydrolysed, independent of their acyl chain length and saturation (Fig. 1h). No change was observed in the amounts of sphingomyelin and triglycerides²¹ (Extended Data Fig. 2c), indicating a specific phospholipase activity towards BMP rather than an overall reduction in lipid abundance during the reaction. Similar results were obtained when lysosomal lipids derived from HEK293T cells were used as substrates incubated with PLA2G15 (Extended Data Fig. 2d–g). Finally, using the synthesized *S,S*BMP, the physiological stereoisomer, we validated the activity of PLA2G15 towards BMP using thin-layer chromatography (Extended Data Fig. 2h). BMP hydrolysis was abolished by the purified PLA2G15 S198A catalytic mutant^{7,22} (Extended Data Fig. 3a–c), as well as in the presence of amiodarone or fosinopril, known inhibitors of phospholipid hydrolysis¹⁸, thus confirming BMP hydrolase activity (Fig. 1i,j). Additionally, we observed no BMP hydrolase activity by purified PLBD2 (Extended Data Fig. 3d–f), an inositol phospholipid preferring lysosomal phospholipase⁷. Taken together, our data indicate that BMP lipids are susceptible to PLA2G15 activity.

sn2, sn2' acylation protects *S,S*BMP from PLA2G15

Although levels of BMP significantly decreased after incubating lysosomal lipids with recombinant PLA2G15, a resistant fraction remained (Fig. 1h and Extended Data Fig. 2f). BMPs can be defined by the acyl chain composition, position and stereochemistry of chiral carbons (Fig. 2a). To gain mechanistic insight into their hydrolysis, we first performed kinetic studies of PLA2G15 activity towards BMPs with different acyl chain lengths under optimum conditions^{7,20} (Extended Data Fig. 4a–d). Consistent with its role as a highly efficient phospholipase B⁷, kinetic analyses of PLA2G15 monitoring the LPG intermediate and GPG product from the first and second steps, respectively, demonstrated high catalytic efficiencies ($k_{\text{cat}}/K_m \approx 10^5\text{--}10^7\text{ M}^{-1}\text{ s}^{-1}$) against two commercially available BMP lipids, which were comparable to those against their phosphatidylglycerol counterparts⁷ (Extended Data Fig. 4e–l). As expected, the first step (Extended Data Fig. 4e–h) was faster than the overall reaction (Extended Data Fig. 4i–l), indicating that the second step controls the rate of the overall reaction⁷. These results established that PLA2G15 is a potent hydrolase of BMP. Although BMP usually displays *S,S* stereoconfiguration, other forms have been isolated, including the *S,R* stereoisomer^{2,23–25} (Fig. 2a). Therefore, we tested PLA2G15 activity against all three potential BMP stereoisomers with the same acyl chains at the primary glycerol carbon positions (*R,R*, *S,R* and *S,S*). All stereoisomers were equally hydrolysed in short-duration experiments (30 s) monitoring LPG release and long-duration experiments (12 h) monitoring the remaining BMP amounts (Fig. 2a,b and Extended Data Fig. 5a). Endogenous BMP can

be acylated either on the secondary carbons sn2, sn2' (2,2' BMP) or primary carbons sn3, sn3' (3,3' BMP) of glycerol^{25,26} (Fig. 2a). Although 3,3' BMP is considered thermodynamically stable and readily synthesized, 2,2' BMP is thought to be a more abundant and physiologically active isoform^{25–28}. To examine BMP hydrolase activity against positional isomers, we obtained synthesized 2,2' BMP and 3,3' BMP standards, both of which contain a small amount of 2,3' positional isomer that can be separated using our mass spectrometry methods and thus leveraged to monitor the stability of all positional isomers (Fig. 2a and Extended Data Fig. 5b). We found a striking reduction in BMP hydrolysis from 2,2' BMP monitoring of the total amounts of BMP after prolonged incubation (12 h) compared to 3,3' BMP (Fig. 2b), despite only a milder difference observed when monitoring LPG release after a short incubation time (30 s) (Extended Data Fig. 5c). A similar observation about the resistance of 2,2' BMP was made when using lysosomal lysates (Fig. 2c). These lysates were derived from cells deficient in CLN5, a known BMP synthase, and thus have very low concentrations of endogenous BMP³. To further understand the hydrolysis of BMP isomers, we monitored the time-dependent total BMP depletion for all isoforms incubated with PLA2G15 (Fig. 2d,e). Consistent with our earlier observation (Fig. 2b and Extended Data Fig. 5a), all three stereoisomers with primary esters were hydrolysed at the same rate (Fig. 2d). However, the hydrolysis rate of 2,2' BMP was much slower than that of 3,3' BMP when incubated with PLA2G15 (Fig. 2e), which indicates that esterification at the secondary carbon contributes to the resistance of BMP to hydrolysis. Consistent with this, we found that the minimal reduction observed in the total BMP in the reaction containing 2,2' BMP was mainly attributed to the hydrolysis of the 2,3' positional isomer (Fig. 2f). We found that LPG released from 2,2' BMP was stable and did not degrade to GPG during the time course experiments (Extended Data Fig. 5d,e), thus explaining why LPG monitoring gave a different result (Extended Data Fig. 5c) and establishing that monitoring LPG release could be misleading in studying the hydrolysis of BMP structural isomers. Additionally, when an equimolar mixture of both synthesized 2,2' and 3,3' BMPs is monitored for total BMP depletion or LPG and GPG release the results resemble the average of each positional isoform, supporting the notion that 3,3' BMP is easily degraded compared to 2,2' BMP (Fig. 2e and Extended Data Fig. 5d,e). Careful analysis of all positional BMP isoform peaks confirmed that 3,3' BMP was quickly degraded, followed by 2,3' BMP, whereas 2,2' BMP was resistant (Fig. 2g,h).

Substrates bind to the enzyme active site for effective catalysis, and BMP is thought to activate lysosomal hydrolases, including PLA2G15²⁹. In silico docking experiments identified a plausible binding pocket that positioned the carbonyl carbon of BMP near the active site of PLA2G15^{7,22} (Extended Data Fig. 5f). BMP binds inactive PLA2G15 (Extended Data Fig. 5g), indicating a similar phospholipase mechanism for BMP by PLA2G15, which involves the serine, aspartate and histidine catalytic triad^{7,22}. Rigorous kinetic analyses monitoring of individual peaks indicated that PLA2G15 has high catalytic efficiency against the 3,3' BMP peak ($k_{\text{cat}}/K_m = 10^7\text{ M}^{-1}\text{ s}^{-1}$), whereas there was no concentration-dependent enzyme activity for the 2,2' BMP peak (Fig. 2i,j and Extended Data Fig. 4d). Finally, hydrolysis of BMP stereoisomers with sn2, sn2' acyl chain positions indicated that both esterification and stereochemistry (2,2' *S,S*) are required for BMP resistance to degradation, because 2,2' BMPs with either *S,R* or *R,R* stereochemistry are readily hydrolysed (Fig. 2k and Extended Data Fig. 5h,i). These results elucidate PLA2G15 as a BMP hydrolase and demonstrate that the characteristic 2,2' esterification position is necessary to protect the physiological *S,S*BMP from hydrolysis.

BMPs accumulate upon PLA2G15 depletion

Several enzymes have been reported to have catabolic activity against BMP in vitro; however, neither has been validated as BMP hydrolase in

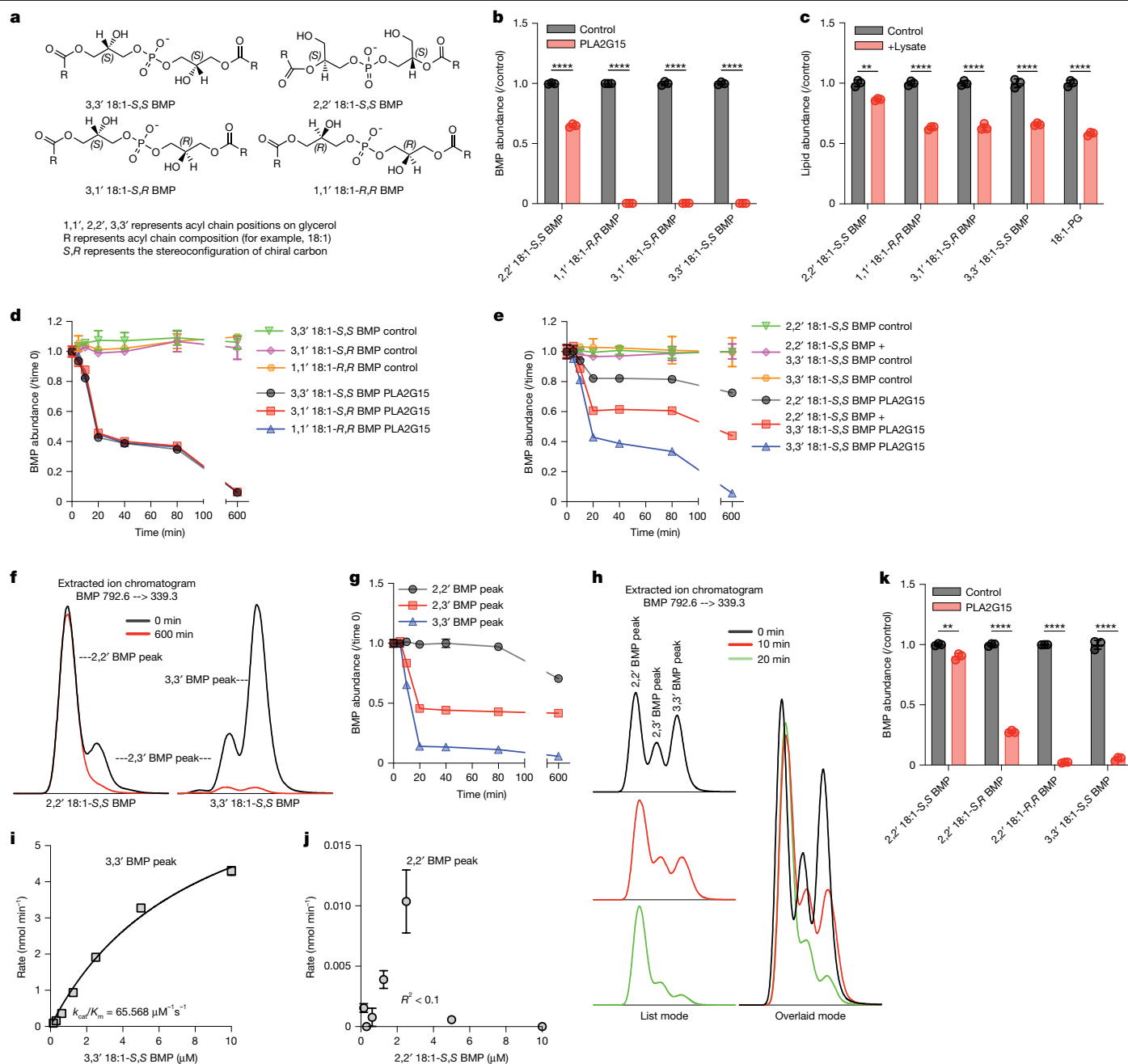


Fig. 2 | sn,sn' esterification position provides S,S BMP with resistance to PLA2G15. a, Chemical structures of the main BMP lipids used in this study. **b**, Hydrolysis of 1 μ M of BMP isomers by 100 nM recombinant PLA2G15 for 12 h (pH 5.0). The control had similar reaction components without the enzyme. Data are presented as mean \pm s.d. of three independent replicates. **** P < 0.0001 by two-tailed unpaired t -tests. **c**, Assay as in **b** for 2 h using 10 μ g of *CLN5* knockout HEK293T lysosomal lysate; n = 3 individual replicates. ** P = 0.0011 and **** P < 0.0001 by two-tailed unpaired t -tests. **d**, Hydrolysis of 20 μ M BMP stereoisomers with primary esters by 100 nM recombinant PLA2G15 over 10 h (pH 5.0). Data are presented as mean \pm s.d. of three independent replicates. **e**, As in **d**, but 20 μ M positional isomers of S,S BMP was used, including a mixture of equimolar amounts. Data are presented as mean \pm s.d. of three independent

replicates. **f**, Representative chromatograms from **e** showing BMP peaks for each isomer in overlaid mode. **g**, Time course analysis from the reaction with an equimolar mixture of 2,2' BMP and 3,3' BMP in **e** showed that the 3,3' peak was preferentially decreased, followed by the 2,3' peak, whereas the 2,2' peak was unchanged. The intensity of each BMP peak was carefully integrated in **g**, and representative chromatograms are shown in **h**. **i,j**, PLA2G15 was incubated with 3,3' 18:1-S,S BMP in **i** and 2,2' 18:1-S,S BMP in **j** for 10 min (pH 5.0). Each experiment was repeated three times, and a representative graph is shown. Data are presented as mean \pm s.d. of three independent replicates. **k**, Assay as in **b** for 1 h using 20 μ M of various BMP isomers. Data are mean \pm s.d. of three independent replicates. ** P = 0.0033 and **** P < 0.0001 by two-tailed unpaired t -tests.

cells or tissues^{5,6,9–11}. Targeted lipidomics revealed a significant increase in almost all BMPs in PLA2G15-deficient HEK293T⁷ lysosomes and cells compared with their wild-type counterparts (Extended Data Fig. 6a,b and Supplementary Table 1). These results were further confirmed in more clones (Fig. 3a,b, Extended Data Fig. 6c and Supplementary

Table 2). Using our established lysosomal enzyme supplementation protocol³, we delivered wild-type or catalytically dead PLA2G15 proteins (Extended Data Fig. 6d,e) to PLA2G15-deficient lysosomes and confirmed that these increases were dependent on the loss of PLA2G15 catalytic activity (Fig. 3c). The amounts of one-fifth of BMP were not

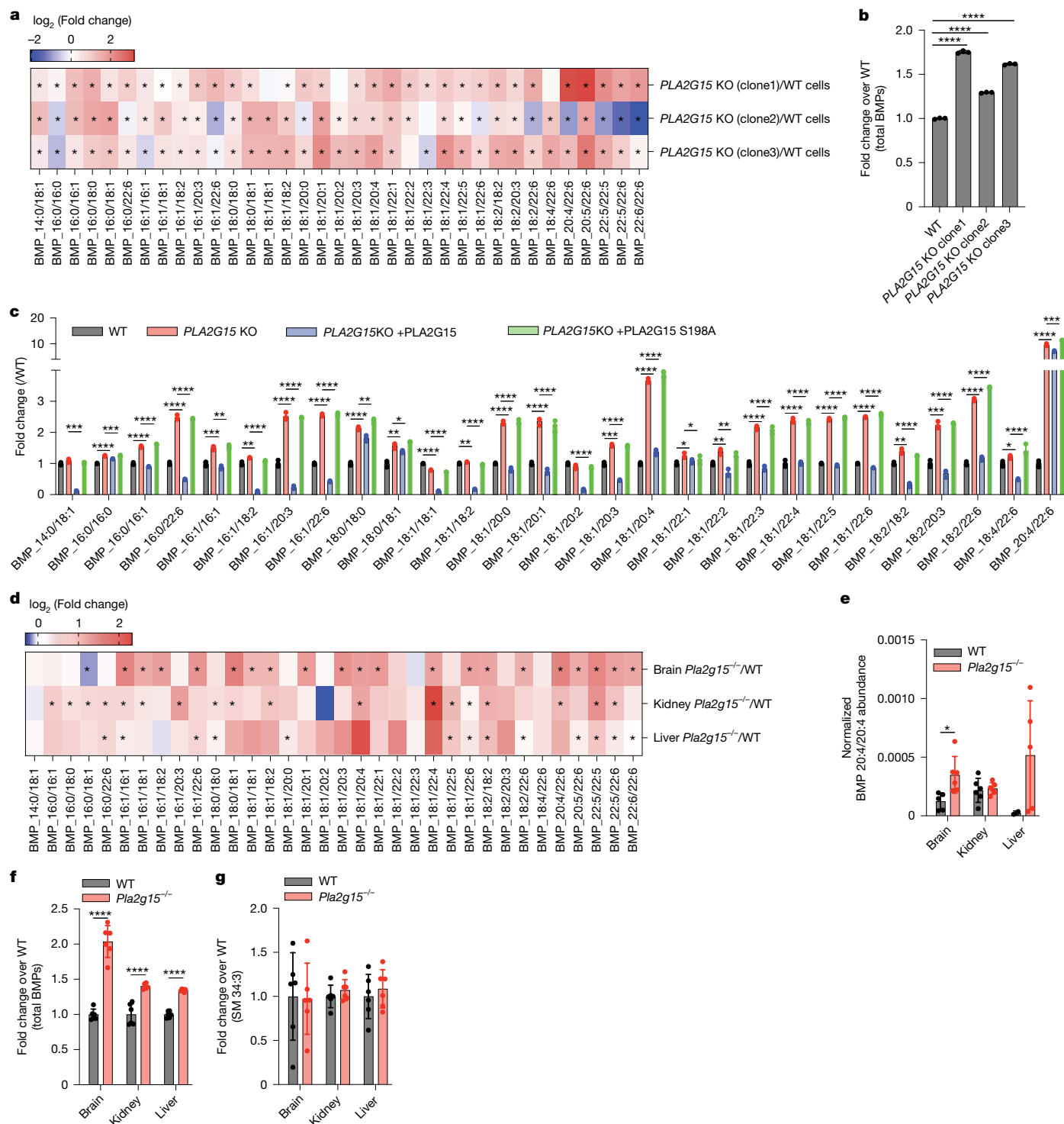


Fig. 3 | PLA2G15-deficient cells and tissues accumulate BMP. **a, b**, Targeted analyses of BMP lipids revealed that a deficiency in PLA2G15 increased BMP amounts in HEK293T cells. **a**, Heat map representation of \log_2 -transformed changes in BMP abundance in PLA2G15-deficient HEK293T cells compared to wild-type controls ($n = 3$ WT and $n = 3$ PLA2G15 knockout (KO)). The data represent the ratio of the mean of each BMP. Significant changes from the graph are represented by $P < 0.05$. P-values were calculated using two-tailed unpaired t -tests and are presented in Supplementary Table 2. **b**, Fold changes in total BMP abundance. Data are presented as mean \pm s.d. Statistical analysis was performed. $****P < 0.0001$ using two-tailed unpaired t -tests. **c**, Recombinant PLA2G15 rescued the elevated concentrations of most BMPs resulting from PLA2G15 loss. Fold changes in BMP concentrations in PLA2G15 knockout HEK293T cells after supplementation with wild-type or mutant PLA2G15 ($n = 3$

independent replicates of each condition). Data are presented as mean \pm s.d. $*P < 0.05$, $**P < 0.01$, $***P < 0.001$ and $****P < 0.0001$ by two-tailed unpaired t -tests. **d**, Heat map representation of \log_2 -transformed changes in BMPs in PLA2G15-deficient mouse tissues compared with their control counterparts ($n = 6$ WT and $n = 6$ PLA2G15 $^{-/-}$). Data are presented as the ratio of the mean of each BMP. $*P < 0.05$ by two-tailed unpaired t -tests and are presented in Supplementary Table 4. **e**, Normalized abundance of BMP 20:4/20:4. This lipid was undetected in some samples; thus, it is reported separately. Data are presented as mean \pm s.d. of six biological replicates. $*P = 0.0157$ using two-tailed unpaired t -tests. **f**, Fold changes in total BMP abundance. Data are presented as mean \pm s.d. of six biological replicates. $****P < 0.0001$ using two-tailed unpaired t -tests. **g**, Fold changes in sphingomyelin (SM 34:3) in the same samples. Data are presented as mean \pm s.d. of six biological replicates.

rescued by PLA2G15, which indicates that either a longer treatment is required or that there may be other enzymes contributing to BMP degradation^{5,6,9–11} (Extended Data Fig. 6f). Many of the non-degraded BMPs have at least one 22:6 acyl chain, which showed a mixed phenotype in the *PLA2G15* knockout clones (Fig. 3a and Supplementary Table 2), indicating an interesting biology that is yet to be discovered^{8,23,25,27}. A recent study indicated that PLA2G15 contributes to BMP synthesis in HeLa cells, although the changes observed were very minimal, if any, and the authors used a knockdown strategy³⁰. Using CRISPR knockout, we found a significant increase in most BMPs of PLA2G15-deficient HeLa cells, whereas 22:6-containing BMPs again showed a mixed phenotype (Extended Data Fig. 6g and Supplementary Table 3). Consistent with our cellular data (Fig. 3a,b), there was a significant increase in most BMPs isolated from the brains, kidneys and livers of PLA2G15-deficient mice compared with their wild-type counterparts (Fig. 3d–f and Supplementary Table 4). Sphingomyelin, a non-glycerophospholipid species, remained mostly unchanged (Fig. 3g and Extended Data Fig. 6h) as previously reported²¹. Although PLA2G15 functions as a phospholipase, there were minimal phospholipid changes, if any, in PLA2G15-deficient lysosomes, cells and even tissues, and changes in hemi-BMP or acyl phosphatidylglycerol concentrations were mixed and insignificant (Extended Data Fig. 6h and Supplementary Table 5). Finally, the concentrations of CLN5, a BMP synthase, and other lysosomal markers did not increase, as did the BMP synthesis in PLA2G15-deficient cells (Extended Data Fig. 6i,j). Thus, PLA2G15 loss of function increased BMP concentrations by reducing its degradation, indicating a vital role for PLA2G15 in BMP hydrolysis and homeostasis.

PLA2G15 regulates lysosomal lipid metabolism

To further validate the role of PLA2G15 activity in regulating BMP homeostasis in the lysosome and the impact of this role on lysosomal function, we first determined that lysosomal lysates from PLA2G15-deficient HEK293T cells indeed have lower degradative activity against BMP (Fig. 4a). Next, we traced the fate of S,S BMP lipids in the presence and absence of PLA2G15 in cells by delivering BMP lipids to lysosomes using established protocols^{3,7,31} (Fig. 4b). We performed *PLA2G15* knockout (Extended Data Fig. 7a) in *CLN5* knockout cells, which exhibit minimal endogenous BMP concentrations, thus allowing tracing of unlabelled exogenously delivered BMP³ (Extended Data Fig. 7b). Liquid chromatography–mass spectrometry (LC–MS) analysis after delivery of either 2,2' BMP or 3,3' BMP to HEK293T cells indicated 2,2' BMP as the major isoform in cells (Extended Data Fig. 7c) as previously reported^{25,27}. Using a pulse-chase approach to track BMP hydrolysis with or without PLA2G15 protein supplementation (Extended Data Fig. 7d,e) following exogenous 2,2' BMP delivery to *CLN5* *PLA2G15* double-knockout cells (Fig. 4b and Extended Data Fig. 7f), we found that BMP was hydrolysed faster in lysosomes with catalytically active PLA2G15 (Fig. 4c and Extended Data Fig. 7g). To determine the effect of esterification position, we delivered either 2,2' BMP or 3,3' BMP and monitored their hydrolysis over time (Fig. 4b,d and Extended Data Fig. 7h,i). Careful peak analysis for 4-h chase following 2,2' BMP delivery showed a moderate 2,2' peak decrease with a concomitant time-dependent increase in both 2,3' and 3,3' peaks (Fig. 4d and Extended Data Fig. 7h), which indicates the need for conversion of 2,2' BMP to 3,3' BMP for effective degradation in cells. Consistent with this notion and our in vitro data (Fig. 2 and Extended Data Fig. 5), the 3,3' and 2,3' peaks from 3,3' BMP rapidly decreased especially in the presence of PLA2G15, whereas conversion of 3,3' BMP to 2,2' BMP was minimal, if any (Fig. 4d and Extended Data Fig. 7h). To confirm this observation and minimize positional isomer conversion, we delivered an equimolar mixture of 2,2' BMP and 3,3' BMP (Fig. 4b,e and Extended Data Fig. 7j). Consistently, we observed rapid degradation of 3,3' and 2,3' BMP compared to 2,2' BMP, confirming that 2,2' BMP is a more resistant BMP isomer (Fig. 4e,f). Notably, 2,2' BMP peak

was not affected by active PLA2G15 (Fig. 4e), which indicates that acyl migration was required for degradation by PLA2G15 (Fig. 4e,f). S,S stereoconfiguration with primary esters (3,3') did not protect BMP from hydrolysis in cells (Extended Data Fig. 7k).

BMP is crucial for lysosomal lipid metabolism, particularly glucocerebrosidase (GCase) activity and cholesterol efflux^{3,16,32–34}. Consistent with PLA2G15 function as a BMP hydrolase, we found that knocking down PLA2G15 significantly upregulated GCase activity in bone marrow-derived macrophages (BMDMs) isolated from wild-type and heterozygous mutant *Gba* D409V mice, although to a lower extent, whereas supplementation with active PLA2G15 decreased GCase activity in BMDMs (Fig. 4g,h and Extended Data Fig. 8a–c). BMP supplementation rescued the cholesterol accumulation phenotype through an NPC2-dependent process in NPC1-deficient cells^{34,35}. Thus, we investigated whether PLA2G15 inhibition could ameliorate cholesterol staining in NPC1 disease models. Consistent with this hypothesis, PLA2G15 was identified as a genetic modifier for NPC1 using a genome-wide haploid genetic screen using cholesterol staining with perfringolysin O (PFO), a bacterial toxin that binds to cholesterol-rich membranes and accumulates in NPC1-deficient cells (Extended Data Fig. 9a–f and Supplementary Table 6). A few lysosomal enzymes differentially regulated cholesterol staining in NPC1-deficient cells (Extended Data Fig. 9d,e). In addition, the screening revealed several genes implicated in cholesterol uptake and efflux as strong regulators, whereas other implicated pathways included glycosylation, organelle contact sites, cargo sorting, clathrin-mediated endocytosis, receptor trafficking/recycling, endosome maturation/trafficking and mitochondrial function^{36–38} (Extended Data Fig. 9a–f and Supplementary Table 6). Consistent with the screening results, RNA interference-mediated knockdown of PLA2G15 reduced cholesterol accumulation in two independent fibroblast lines of patients with NPC1 using filipin staining as an orthogonal approach to detect cholesterol (Fig. 4i,j and Extended Data Fig. 8d). These data indicate that PLA2G15 regulates lysosomal lipid metabolism, and its inhibition can ameliorate disease-related lysosomal lipid dyshomeostasis.

Targeting *Pla2g15* reverses NPC1 defects

On the basis of these data, we tested whether PLA2G15 depletion has therapeutic value in NPC1 disease. To this end, we generated PLA2G15-deficient mice and crossed them with *Npc1*^{min}/J mice, a model that exhibits severe central nervous system (CNS) and peripheral NPC characteristics. First, we measured well-established disease biomarkers, including neurofilament light chain (NFL) in the cerebrospinal fluid (CSF) and plasma for neurodegeneration and aspartate aminotransferase (AST) and alanine aminotransferase (ALT) for liver damage^{39–41}. Depletion of PLA2G15 in NPC1-deficient mice significantly reversed these disease biomarkers (Fig. 5a,b). NPC1 models displayed increased BMP concentrations⁴²; thus, PLA2G15 depletion showed only a slight increase in a few BMP species, if any, consistent with a potential cell-type specific effect³³, or a net effect driven by reduced lysosomal stress in NPC1 lysosomes in the double-knockout mice (Extended Data Fig. 10a and Supplementary Table 7). PLA2G15 loss of function did not significantly alter the cholesterol levels detected in the brains or livers. However, elevated secondary storage lipids, including sphingolipids and alkyl-lysophosphatidylcholine, were significantly reduced in both tissues^{38,43,44} (Extended Data Fig. 10b–d and Supplementary Table 8). NPC1 deficiency profoundly affects Purkinje neuron survival and development, triggers glial reactivity and affects several organ systems^{45–48}. Depletion of PLA2G15 in NPC1-deficient mice significantly alleviated neuropathological findings, such as Purkinje cell loss, astrogliosis, microgliosis and demyelination across the CNS (Fig. 5c–f, Extended Data Fig. 10e,f and Supplementary Table 9). In addition, inhibition of PLA2G15 reduced

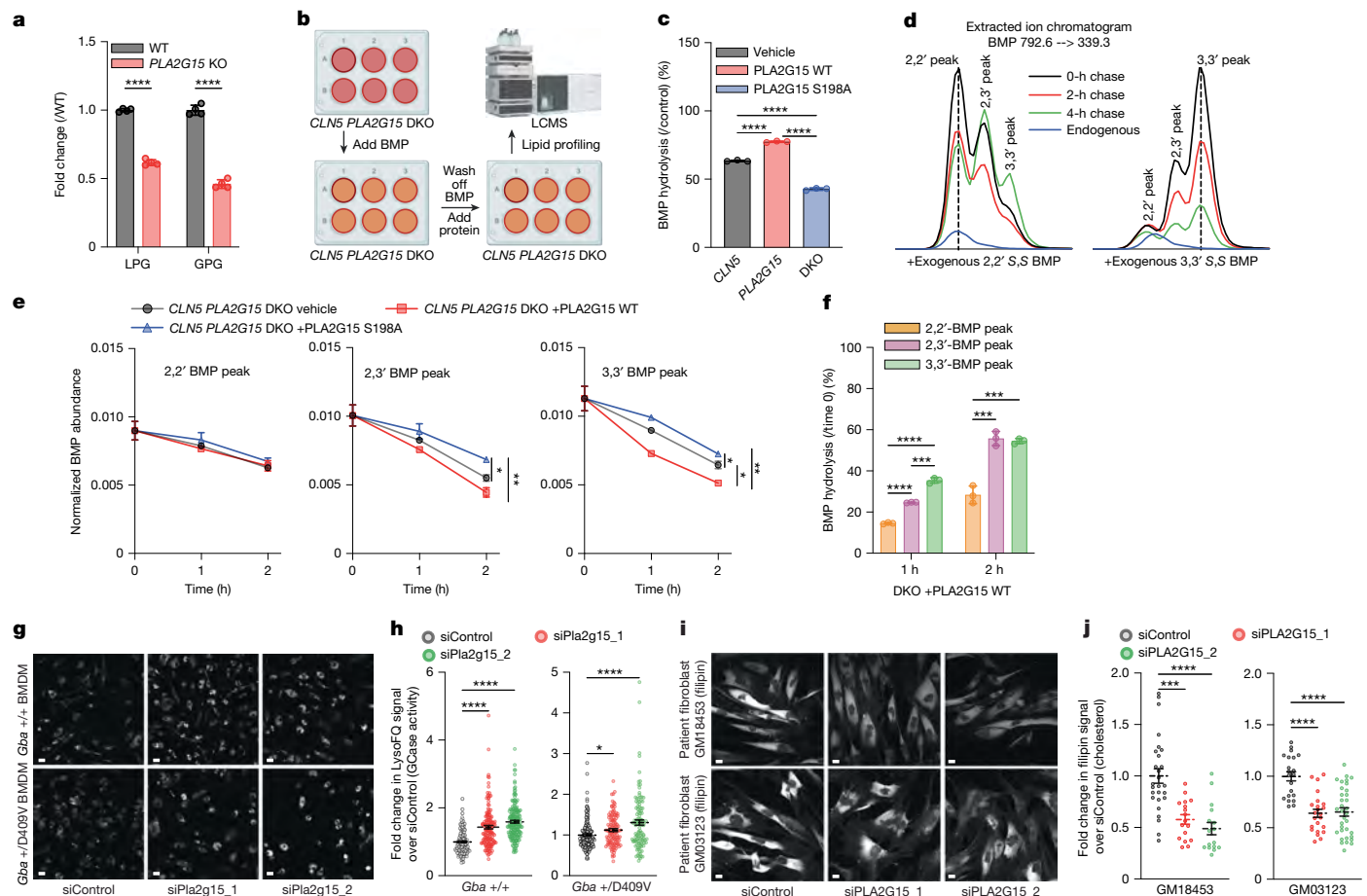


Fig. 4 | PLA2G15 regulates lysosomal lipid metabolism. **a**, Hydrolysis of 1 μ M 3,3',S-BMP by 5 μ g wild-type or PLA2G15 knockout lysosomal lysates for 10 min (pH 5.0). Data are presented as mean \pm s.d. of three individual replicates. **** P < 0.0001 using two-tailed unpaired t -tests. **b**, Pulse-chase experimental design. **c**, Cells were treated with 10 μ M 2,2',S BMP for 2 h, washed and chased with phosphate-buffered saline (PBS) (vehicle) or 100 nM protein for 2 days. Data are mean \pm s.d. of three individual replicates. **** P < 0.0001 using two-tailed unpaired t -tests. **d**, Representative chromatograms during a 4-h wild-type PLA2G15 chase after delivering the indicated BMPs. **e**, Indicated BMP peaks were measured following a 2-h chase with PLA2G15 proteins after the addition of equimolar 2,2',S and 3,3',S BMP mixture for 2 h. Data are presented as mean \pm s.d. of three individual replicates. * P < 0.05 and ** P < 0.01 by two-way analysis of variance (ANOVA) with Tukey's test. **f**, Quantification of BMP peaks from **e** during wild-type PLA2G15 chase. Data are presented as mean \pm s.d. of

three individual replicates. *** P < 0.001 and **** P < 0.0001 using two-tailed unpaired t -tests. **g**, Representative images of 3-day small interfering RNA (siRNA)-treated BMDMs after LysoFQ-GBA incubation. **h**, Quantification of LysoFQ-GBA intensity. Data are presented as mean \pm s.e.m. *Gba*^{+/+}: siControl, n = 174 cells; siPLA2G15_1, n = 153 cells; siPLA2G15_2, n = 185 cells. *Gba*^{+/-}: siControl, n = 170 cells; siPLA2G15_1, n = 119 cells; siPLA2G15_2, n = 112 cells. * P = 0.0336 and **** P < 0.0001 by one-way ANOVA with Fisher's least significant difference (LSD) test. **i**, Representative images of filipin-stained fibroblasts from patients with NPC1 after 2-day siRNA treatment. **j**, Quantification of filipin intensity. Data are mean \pm s.e.m. siControl, n = 27 cells; siPLA2G15_1, n = 17 cells; siPLA2G15_2, n = 16 cells. GM03123: siControl, n = 21 cells; siPLA2G15_1, n = 23 cells; siPLA2G15_2, n = 34 cells. *** P = 0.0003 and **** P < 0.0001 by one-way ANOVA with Kruskal–Wallis test. Scale bars, 20 μ m (**g**, **i**). Panel **b** was created using BioRender (<https://biorender.com>).

hyperplasia in Kupffer cells from NPC1-deficient livers, whereas vacuolation in hepatocytes remained unaltered (Extended Data Fig. 10g,h). Similarly, inhibition of PLA2G15 reduced the hyperplasia of histocytes and lymphoid atrophy in NPC1-deficient spleens, whereas histological findings observed in the lungs were not corrected (Extended Data Fig. 10g,h). Notably, histopathological and histomorphometric evaluations of the CNS, livers, spleens and lungs revealed no lesions in PLA2G15-deficient mice compared to those in control mice (Fig. 5c–f and Extended Data Fig. 10g,h). Consistently, genetically targeting PLA2G15 strongly improved the neurological composite score and ataxia symptoms in NPC1-deficient mice, leading to a significantly extended lifespan of diseased mice⁴⁵ (Fig. 5g–i and Extended Data Fig. 10i). These data indicate that PLA2G15 depletion reduces neurodegeneration in the brain and defects in visceral organs of NPC1-deficient mice. Overall, these results, in conjunction with our in vitro and in vivo data, indicate that PLA2G15 possesses a BMP hydrolase activity that is required for BMP homeostasis in the lysosome, and its targeting can

boost BMP-mediated functions and lysosomal activity in diseases with lysosomal dysfunction.

Discussion

BMP is a unique lipid known to potentially stimulate lysosome-mediated lipid turnover, a crucial cellular process that, when defective, leads to a plethora of human diseases, including neurodegeneration^{1,2}. Despite its therapeutic potential in targeting the BMP pathway and its significant functions in lysosomes, little is known about BMP synthesis and degradation^{1,2}. We recently discovered CLN5 as a BMP synthase in lysosomes. However, the rules governing BMP stability and the enzymes that mediate its hydrolysis, if any, are yet to be identified. For more than 50 years, it has been believed that lysosomes do not have a BMP hydrolase or that the unique stereochemistry of BMP (S,S) alone is protective from such a hydrolase if it exists⁸. To challenge both assumptions, we identified lysosomal phospholipase PLA2G15 as an efficient

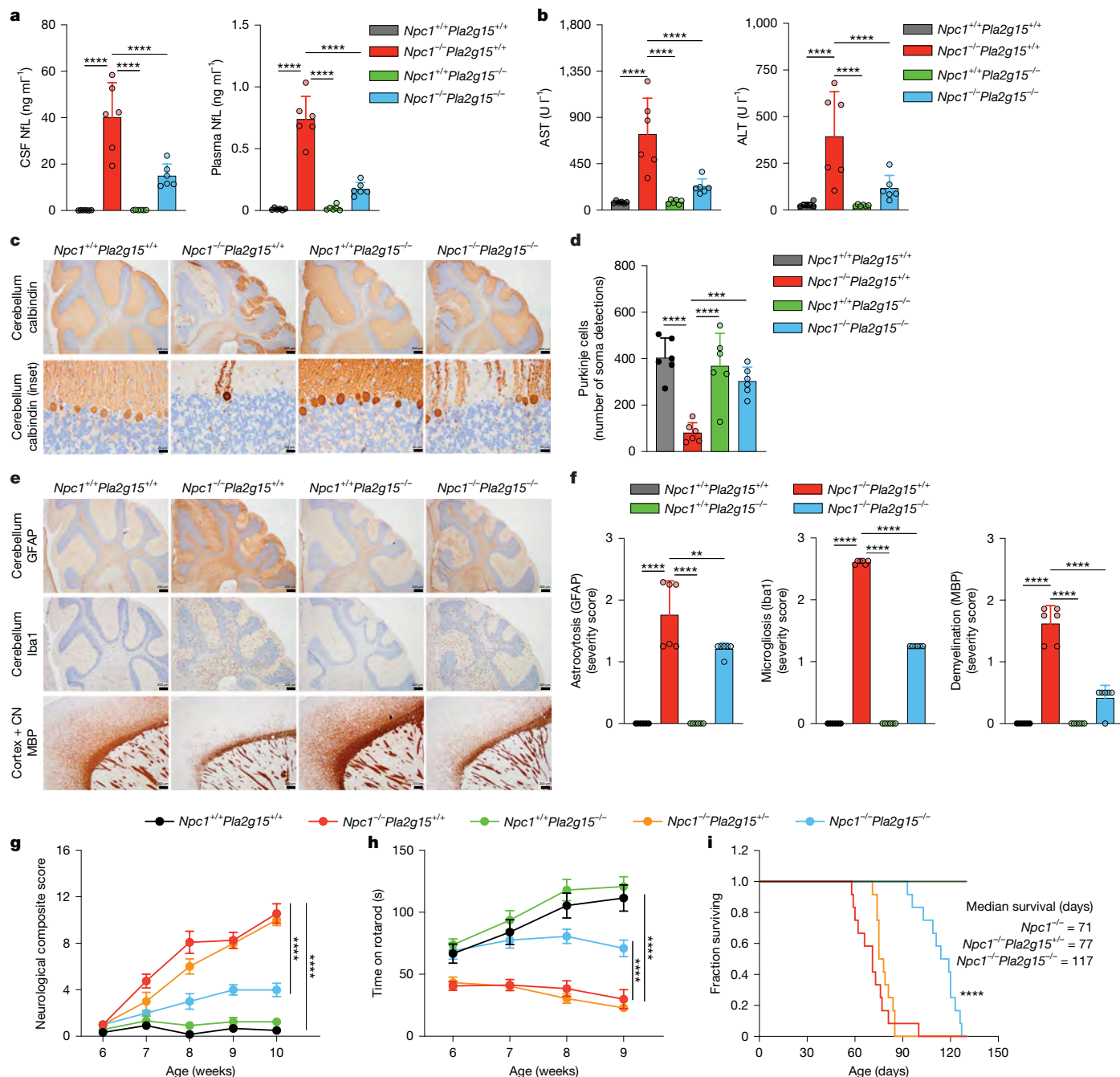


Fig. 5 | Genetic ablation of *Pla2g15* ameliorates disease symptoms and extends lifespan in NPC1-deficient mouse. **a, b**, PLA2G15 depletion rescued the elevated levels of neurodegenerative and liver damage biomarkers in NPC1-deficient mice. NFL concentrations in the CSF (left) and plasma (right) (**a**) and plasma concentrations of liver transaminases AST (left) and ALT (right) (**b**) measured on day 56. Data are presented as mean \pm s.d. ($n = 6$, that is, three male and three female mice per genotype). * $P < 0.05$, ** $P < 0.01$, *** $P < 0.001$ and **** $P < 0.0001$ by one-way ANOVA with Fisher's LSD test. **c–f**, Genetic depletion of PLA2G15 increased Purkinje cell survival (**c, d**) and decreased astrocytosis, microgliosis and demyelination (**e, f**) in the CNS of NPC1-deficient mice. Representative images are shown in **c, e**. Histomorphometry to quantify the number of Purkinje cells per slide and the mean severity score (Methods) of the histopathological evaluation are shown in **d** and **f**, respectively. Data are mean \pm s.d. ($n = 6$, that is, three male and three female mice per genotype).

** $P = 0.0025$, *** $P = 0.0004$ and **** $P < 0.0001$ by one-way ANOVA comparing NPC1-deficient tissues with other genotypes. **g–i**, Genetic depletion of PLA2G15 improved neurological composite (Methods) score (**g**) and motor defect (**h**) and increased survival rate (**i**) in NPC1-deficient mice. Data are presented as mean \pm s.e.m. of 12 mice (six male and six female mice per genotype). In **h**, ataxia symptoms were measured using a rotarod. Data are presented as mean \pm s.e.m. of 12 mice (six male and six female mice per genotype). **** $P < 0.0001$ by two-way ANOVA comparing *Npc1^{-/-}Pla2g15^{+/+}* to either *Npc1^{-/-}Pla2g15^{-/-}* or *Npc1^{+/+}Pla2g15^{+/+}*. **i**, Kaplan–Meier graph for animal survival. Data from $n = 12$, that is, six male and six female mice per genotype. The curves for *Npc1^{+/+}Pla2g15^{+/+}* and *Npc1^{+/+}Pla2g15^{-/-}* completely overlap. **** $P < 0.0001$ by log-rank (Mantel–Cox) test. Scale bars, 200 μ m, except 20 μ m for the cerebellar calbindin inset (**a–i**). CN, cerebral nuclei.

BMP hydrolase regardless of stereoconfiguration if BMP has primary esters, contrary to a recent report⁴⁹. We found that the sn2, sn2' (2,2' BMP) esterification position, another unique feature of BMP, along

with the *S,S* stereoconfiguration, shields BMP from lysosomal degradation, facilitated in part by PLA2G15. These results indicate that acyl migration within the BMP molecule is an active process that allows

regulated turnover of BMP in lysosomes. We observed that 2,2' BMP was converted into 2,3' BMP and 3,3' BMP, both of which are susceptible to PLA2G15 activity. Although this conversion is thermodynamically favoured, we still found 2,2' BMP to be more abundant than 3,3' BMP in the lysosome, consistent with the notion that it is the biologically active form^{25–28}. We speculate that BMP stability is maintained by an unidentified biological machinery that protects its 2,2' BMP isoform from acyl migration¹. Future studies should investigate the preferential synthesis or preservation of 2,2' BMP. Consistent with these biochemical findings, loss of PLA2G15 led to the accumulation of BMP lipids in cells and tissues, whereas most other phospholipids were unchanged. However, it has been reported that PLA2G15-deficient mice displayed splenomegaly and phospholipidosis in alveolar macrophages with age, reduced presentation of lysophospholipid antigens to CD1d by invariant natural killer T cells and impaired adaptive T cell immunity against *Mycobacterium*^{50–52}.

Consistent with the role of BMP in promoting lysosomal functions, such as lipid degradation and cholesterol trafficking^{1–3,29,32,34}, we showed that inhibiting and supplementing PLA2G15 to BMDMs upregulated and reduced GCase activity, respectively, whereas depleting PLA2G15 reduced cholesterol accumulation in patient-derived NPC1-deficient fibroblasts. We found that genetic depletion of PLA2G15 ameliorated most but not all NPC1 defects, including secondary and primary lipid storage, neurodegeneration, spleen and liver damage, leading to improved neurological symptoms and survival in an NPC1-deficient mouse model^{39–41,45–48}. These data indicate that inhibiting PLA2G15 represents a potential therapeutic strategy to boost BMP concentrations and treat several lysosome-related diseases. This observation is consistent with the BMP therapeutic hypothesis that we recently proposed on the basis of studies conducted by many others¹.

In summary, our study identified PLA2G15 as a key hydrolase that actively degrades BMP in lysosomes and established rules that protect BMP from lysosomal hydrolysis, thus resolving the long-standing mystery of how the unique characteristics of BMP mediate its functions. These insights pave the way for new therapeutic strategies targeting the BMP pathway in diseases in which it is disrupted.

Online content

Any methods, additional references, Nature Portfolio reporting summaries, source data, extended data, supplementary information, acknowledgements, peer review information; details of author contributions and competing interests; and statements of data and code availability are available at <https://doi.org/10.1038/s41586-025-08942-y>.

- Medoh, U. N. & Abu-Remaileh, M. The bis(monoacylglycerol)-phosphate hypothesis: from lysosomal function to therapeutic avenues. *Annu. Rev. Biochem.* <https://doi.org/10.1146/annurev-biochem-092823-113814> (2024).
- Showalter, M. R. et al. The emerging and diverse roles of bis(monoacylglycerol) phosphate lipids in cellular physiology and disease. *Int. J. Mol. Sci.* **21**, 8067 (2020).
- Medoh, U. N. et al. The Batten disease gene product CLN5 is the lysosomal bis(monoacylglycerol)phosphate synthase. *Science* **381**, 1182–1189 (2023).
- Bulfon, D. et al. Functionally overlapping intra- and extralysosomal pathways promote bis(monoacylglycerol)phosphate synthesis in mammalian cells. *Nat. Commun.* **15**, 9937 (2024).
- Huterer, S. & Wherrett, J. R. Deacylation of bis(monoacylglycerol)phosphate by lysosomal and microsomal lysophospholipases from rat liver. *Can. J. Biochem.* **60**, 599–607 (1982).
- Pribasnig, M. A. et al. α/β Hydrolase domain-containing 6 (ABHD6) degrades the late endosomal/lysosomal lipid bis(monoacylglycerol)phosphate. *J. Biol. Chem.* **290**, 29869–29881 (2015).
- Nyame, K. et al. Glycerophosphodiesterases inhibit lysosomal phospholipid catabolism in Batten disease. *Mol. Cell.* <https://doi.org/10.1016/j.molcel.2024.02.006> (2024).
- Weglicki, W. B., Ruth, R. C. & Owens, K. Changes in lipid composition of tritosomes during lysis. *Biochem. Biophys. Res. Commun.* **51**, 1077–1082 (1973).
- Ito, M., Tchoua, U., Okamoto, M. & Tojo, H. Purification and properties of a phospholipase A₂/lipase preferring phosphatidic acid, bis(monoacylglycerol) phosphate, and monoacylglycerol from rat testis. *J. Biol. Chem.* **277**, 43674–43681 (2002).
- Record, M. et al. Bis (monoacylglycerol) phosphate interfacial properties and lipolysis by pancreatic lipase-related protein 2, an enzyme present in THP-1 human monocytes. *Biochim. Biophys. Acta* **1811**, 419–430 (2011).
- Matsuzawa, Y. & Hostetler, K. Y. Degradation of bis(monoacylglycerol)phosphate by an acid phosphodiesterase in rat liver lysosomes. *J. Biol. Chem.* **254**, 5997–6001 (1979).
- Abe, A. et al. The secretion and uptake of lysosomal phospholipase A₂ by alveolar macrophages. *J. Immunol.* **181**, 7873–7881 (2008).
- Abe, A., Hinkovska-Galcheva, V., Bouchev, P., Bouley, R. & Shayman, J. A. The role of lysosomal phospholipase A2 in the catabolism of bis(monoacylglycerol)phosphate and association with phospholipidosis. *J. Lipid Res.* **65**, 100574 (2024).
- Abu-Remaileh, M. et al. Lysosomal metabolomics reveals V-ATPase- and mTOR-dependent regulation of amino acid efflux from lysosomes. *Science* **358**, 807–813 (2017).
- Wherrett, J. R. & Huterer, S. Enrichment of bis-(monoacylglycerol) phosphate in lysosomes from rat liver. *J. Biol. Chem.* **247**, 4114–4120 (1972).
- Kobayashi, T. et al. Late endosomal membranes rich in lysobisphosphatidic acid regulate cholesterol transport. *Nat. Cell Biol.* **1**, 113–118 (1999).
- Laqtom, N. N. et al. CLN3 is required for the clearance of glycerophosphodiesterases from lysosomes. *Nature* **609**, 1005–1011 (2022).
- Hinkovska-Galcheva, V. et al. Inhibition of lysosomal phospholipase A2 predicts drug-induced phospholipidosis. *J. Lipid Res.* **62**, 100089 (2021).
- Baritussio, A. et al. Amiodarone inhibits lung degradation of SP-A and perturbs the distribution of lysosomal enzymes. *Am. J. Physiol. Lung Cell. Mol. Physiol.* **281**, L1189–L1199 (2001).
- Hinkovska-Galcheva, V. et al. Determinants of pH profile and acyl chain selectivity in lysosomal phospholipase A₂. *J. Lipid Res.* **59**, 1205–1218 (2018).
- Shayman, J. A. & Tesmer, J. J. G. Lysosomal phospholipase A2. *Biochim. Biophys. Acta, Mol. Cell. Biol. Lipids* **1864**, 932–940 (2019).
- Bouley, R. A., Hinkovska-Galcheva, V., Shayman, J. A. & Tesmer, J. J. G. Structural basis of lysosomal phospholipase A₂ inhibition by Zn²⁺. *Biochemistry* **58**, 1709–1717 (2019).
- Joutti, A., Brothier, J., Renkonen, O., Laine, R. & Fischer, W. The stereochemical configuration of lysobisphosphatidic acid from rat liver, rabbit lung and pig lung. *Biochim. Biophys. Acta* **450**, 206–209 (1976).
- Joutti, A. The stereochemical configuration of newly formed molecules of bis(monoacylglycerol) phosphate in BHK cells. *Biochim. Biophys. Acta* **575**, 10–15 (1979).
- Luquain, C. et al. Bis(monoacylglycerol) phosphate in rat uterine stromal cells: structural characterization and specific esterification of docosahexaenoic acid. *Biochem. J.* **351**, 795–804 (2000).
- Luquain, C., Laugier, C., Lagarde, M. & Pageaux, J. F. High-performance liquid chromatography determination of bis(monoacylglycerol) phosphate and other lysophospholipids. *Anal. Biochem.* **296**, 41–48 (2001).
- Kobayashi, T. et al. Separation and characterization of late endosomal membrane domains. *J. Biol. Chem.* **277**, 32157–32164 (2002).
- Chevallier, J. et al. Lysobisphosphatidic acid controls endosomal cholesterol levels. *J. Biol. Chem.* **283**, 27871–27880 (2008).
- Abe, A. & Shayman, J. A. The role of negatively charged lipids in lysosomal phospholipase A2 function. *J. Lipid Res.* **50**, 2027–2035 (2009).
- Chen, J. et al. Lysosomal phospholipase A2 contributes to the biosynthesis of the atypical late endosome lipid bis(monoacylglycerol)phosphate. *Commun. Biol.* **6**, 210 (2023).
- Scharenberg, S. G. et al. An SPNS1-dependent lysosomal lipid transport pathway that enables cell survival under choline limitation. *Sci. Adv.* **9**, eadf8966 (2023).
- Logan, T. et al. Rescue of a lysosomal storage disorder caused by Grn loss of function with a brain penetrant progranulin biologic. *Cell* **187**, 1565–1566 (2024).
- Bennett, M. L. et al. New tools for studying microglia in the mouse and human CNS. *Proc. Natl Acad. Sci. USA* **113**, E1738–E1746 (2016).
- McCaulliff, L. A. et al. Intracellular cholesterol trafficking is dependent upon NPC2 interaction with lysobisphosphatidic acid. *eLife* **8**, e50832 (2019).
- Illytska, O. et al. Enrichment of NPC1-deficient cells with the lipid LBPA stimulates autophagy, improves lysosomal function, and reduces cholesterol storage. *J. Biol. Chem.* **297**, 100813 (2021).
- Ory, D. S. The Niemann-Pick disease genes: regulators of cellular cholesterol homeostasis. *Trends Cardiovasc. Med.* **14**, 66–72 (2004).
- Colaco, A. et al. Unbiased yeast screens identify cellular pathways affected in Niemann-Pick disease type C. *Life Sci. Alliance* **3**, e201800253 (2020).
- Vanier, M. T. Complex lipid trafficking in Niemann-Pick disease type C. *J. Inher. Metab. Dis.* **38**, 187–199 (2015).
- Agrawal, N. et al. Neurofilament light chain in cerebrospinal fluid as a novel biomarker in evaluating both clinical severity and therapeutic response in Niemann-Pick disease type C1. *Genet. Med.* **25**, 100349 (2023).
- Dardis, A. et al. Plasma neurofilament light (NfL) in patients affected by Niemann-Pick type C disease (NPCD). *J. Clin. Med.* **10**, 4796 (2021).
- Garver, W. S. et al. Characterization of liver disease and lipid metabolism in the Niemann-Pick C1 mouse. *J. Cell. Biochem.* **101**, 498–516 (2007).
- Vanier, M. T. Biochemical studies in Niemann-Pick disease. I. Major sphingolipids of liver and spleen. *Biochim. Biophys. Acta* **750**, 178–184 (1983).
- Praggastis, M. et al. A murine Niemann-Pick C11061T knock-in model recapitulates the pathological features of the most prevalent human disease allele. *J. Neurosci.* **35**, 8091–8106 (2015).
- Mishra, S. et al. Accumulation of alkyl-lysophosphatidylcholines in Niemann-Pick disease type C1. *J. Lipid Res.* **65**, 100600 (2024).
- Santiago-Mujica, E. et al. Hepatic and neuronal phenotype of NPC1^{-/-} mice. *Heliyon* **5**, e01293 (2019).
- Ko, D. C. et al. Cell-autonomous death of cerebellar Purkinje neurons with autophagy in Niemann-Pick type C disease. *PLoS Genet.* **1**, 81–95 (2005).
- Lopez, M. E., Klein, A. D., Dimbil, U. J. & Scott, M. P. Anatomically defined neuron-based rescue of neurodegenerative Niemann-Pick type C disorder. *J. Neurosci.* **31**, 4367–4378 (2011).

48. Xie, C., Gong, X. M., Luo, J., Li, B. L. & Song, B. L. AAV9-NPC1 significantly ameliorates Purkinje cell death and behavioral abnormalities in mouse NPC disease. *J. Lipid Res.* **58**, 512–518 (2017).
49. Singh, S. et al. PLD3 and PLD4 synthesize S,S-BMP, a key phospholipid enabling lipid degradation in lysosomes. *Cell* **187**, 6820–6834.e6824 (2024).
50. Schneider, B. E. et al. Lysosomal phospholipase A₂: a novel player in host immunity to *Mycobacterium tuberculosis*. *Eur. J. Immunol.* **44**, 2394–2404 (2014).
51. Paduraru, C. et al. Role for lysosomal phospholipase A2 in iNKT cell-mediated CD1d recognition. *Proc. Natl Acad. Sci. USA* **110**, 5097–5102 (2013).
52. Hiraoka, M. et al. Lysosomal phospholipase A2 and phospholipidosis. *Mol. Cell. Biol.* **26**, 6139–6148 (2006).

Publisher's note Springer Nature remains neutral with regard to jurisdictional claims in published maps and institutional affiliations.



Open Access This article is licensed under a Creative Commons Attribution-NonCommercial-NoDerivatives 4.0 International License, which permits any non-commercial use, sharing, distribution and reproduction in any medium or format, as long as you give appropriate credit to the original author(s) and the source, provide a link to the Creative Commons licence, and indicate if you modified the licensed material. You do not have permission under this licence to share adapted material derived from this article or parts of it. The images or other third party material in this article are included in the article's Creative Commons licence, unless indicated otherwise in a credit line to the material. If material is not included in the article's Creative Commons licence and your intended use is not permitted by statutory regulation or exceeds the permitted use, you will need to obtain permission directly from the copyright holder. To view a copy of this licence, visit <http://creativecommons.org/licenses/by-nc-nd/4.0/>.

© The Author(s) 2025

Methods

Chemicals and antibodies

The antibodies and chemicals used in this study with their details are listed in Supplementary Table 10.

Plasmids

Plasmids (wild-type PLA2G15-6xHis and PLA2G15-6xHis S198A) were obtained from a previous study, with Addgene IDs 213603 and 213605, respectively⁷.

Animal studies

Mice were acquired and maintained, as previously described¹⁷. The mice were housed in a controlled environment with regulated 20–26 °C temperature and 30–70% relative humidity, 12-h light/dark cycles and access to food and water. Supplies were checked daily, and the cages were cleaned every 4–5 days. All mouse procedures were conducted in accordance with the approved guidelines of the Administrative Panel on Laboratory Animal Care at Stanford University. The LysoTag mouse was previously reported (Jackson Laboratory (JAX); strain no. 035401)¹⁷. *Gba*^{D409V} was obtained from JAX (strain no. 019106)⁵³. PLA2G15-deficient mice were obtained, housed and used in accordance with approved Institutional Animal Care and Use Committee protocols at the University of Wisconsin–Madison^{52,54}. Before euthanasia and necropsy, the PLA2G15-deficient mice were fasted for 6 h.

Mouse genotypes were confirmed by pPCR using DirectPCR (Thermo Fisher Scientific; AA4647500) according to the manufacturer's guidelines. Briefly, tail clippings were incubated in DirectPCR overnight at 60 °C for 16 h, followed by the addition of proteinase K and further incubation for 1 h. PCR was performed with PLA2G15 primers (Pla2g15_1: 5'-GAATTCCTAGACCCAGCAAGAGGAATGTG-3'; Pla2g15_2: 5'-ACTGCTCCCCCTCCCCAGAGATGGATATT-3') using a program of 4 min at 95 °C, followed by 35 cycles of 1 min at 95 °C, 1 min at 55 °C, 1 min at 72 °C and finally with an 8-min incubation at 72 °C. The results of genotyping were validated using reverse transcription PCR (RT–PCR) and western blotting of the excised tissue. These mice were used in experiments, as shown in Fig. 3. For all animal studies, the samples were randomized and blinded when possible, with all sample sizes, sexes and ages detailed in the legends and/or related supplementary tables.

Generation of *Pla2g15*^{−/−} mice for the NPC1 rescue experiment

Constitutive *Pla2g15*^{−/−}(TAC) mice were obtained through CRISPR–Cas9-mediated gene editing at Taconic Biosciences in accordance with national and international regulations. Animal procedures were evaluated by veterinarians and Taconic's Institutional Animal Care and Use Committee or an equivalent oversight body to ensure the elimination or minimization of the potential for pain or distress. The gene targeting strategy was on the basis of the National Center for Biotechnology Information (NCBI) transcript NM_133792.3 (*Pla2g15*) and was designed to delete exon 3 from the transcript (proximal single guide RNA (sgRNA): 5'-TCGATGCCATTCATGGACTT-3' and distal sgRNA: 5'-GGCCTACTACGTTGCTTTGA-3'), resulting in the loss of function of PLA2G15 by generating a frameshift from exon 2 to all downstream exons and creating a premature stop codon in exon 4.

Pla2g15 exon 3 flanking primers (forward: 5'-ACTCACTTATAGAC CAGGTTGGC-3' and reverse: 5'-CAGAGACAGTGAACCTAAGGGC-3') were designed to amplify and confirm both wild-type and edited *Pla2g15* alleles.

In brief, Cas9 protein and sgRNAs were injected into BALB/c zygotes, and G0 animals were genotyped by PCR analysis, as described above. Founders were identified and used for further breeding activities to create heterozygous *Pla2g15*^{−/−}(TAC) mice. These mice were subsequently used to generate homozygous *Pla2g15*^{−/−}(TAC) mice, which were used in experiments, as shown in Fig. 5.

Lifespan analysis and neurological phenotyping

Pla2g15^{−/−}(TAC) BALB/c mice were crossed with *Npc1*^{miN}/J heterozygous animals (JAX no. 003092), and from the resulting offspring, double-HET mice were used to obtain the following genotypes (gene order: *Npc1*^{miN}/J/*Pla2g15*): wild type/wild type, homozygous/wild type, homozygous/heterozygous, homozygous/knockout and wild type/knockout. Wild type represents *Npc1*^{+/+} or *Pla2g15*^{+/+}, knockout represents *Npc1*^{+/+}*Pla2g15*^{−/−}, HOM represents *Npc1*^{−/−}*Pla2g15*^{+/+} and heterozygous represents *Pla2g15*^{+/−}. In total, 60 animals were included in the phenotypic analysis, with 12 mice of each of the different genotypes (six male and six female mice). The body weights of all mice were assessed every other day starting at 3 weeks of age after the pups were weaned. Motor coordination was assessed weekly using the rotarod test from 6 to 9 weeks of age. The neurological composite phenotype score, consisting of the ledge test, hindlimb clasping, gait, kyphosis, tremor and grooming scores, was performed on a weekly basis starting at 6 weeks of age. These tests were performed according to an established protocol⁵⁵. A higher composite score indicates worse neurological performance and was calculated using hindlimb clasping, grooming, tremor, gait, kyphosis and ledge test. Starting at 8 weeks of age, all animals carrying the *Npc1*^{miN}/J HOM genotype were subjected to daily monitoring of clinical signs or termination criteria scoring, along with special care (such as providing wet food), which exceeded the standard health checks and animal care. Experiments were performed at QPS Austria in compliance with the Animal Care and Welfare Committee and animal welfare regulations from local authorities.

CSF and plasma analysis

At 8 weeks of age (postnatal day 56 ± 2 days), the mice were terminally anaesthetized by intraperitoneal injection of pentobarbital (600 mg kg^{−1}), and CSF and blood plasma were obtained. The NFL levels were assessed using ELISA 10-7001 CE from UmanDiagnostics in plasma and CSF. Plasma samples were diluted 1:3 and CSF 1:30 (wherever possible) in the assay buffer and analysed according to the manufacturer's protocol.

AST and ALT concentrations were measured using commercial kits (catalogue nos. 04467493190 and 04467388190, respectively; Roche), according to the International Federation of Clinical Chemistry and Laboratory Medicine with pyridoxal phosphate activation (Roche). Therefore, kinetic measurement of the enzyme activity with a redox reaction of nicotinamide adenine dinucleotide hydrogen was performed using L-aspartate and 2-oxoglutarate as substrates for AST measurement and L-alanine and 2-oxoglutarate as substrates for ALT measurement. The concentrations of the two enzymes were measured using a Roche cobas 6000/c501 analyser.

Histoprocessing

The CNS, livers, spleens and lungs of all animals were sampled at necropsy, frozen and transferred to AnaPath Services GmbH for histoprocessing. The samples were placed in formalin, embedded in paraffin wax and cut to a nominal thickness of 4 µm. The livers, spleens and lungs were stained with haematoxylin and eosin. In the CNS, five sagittal serial sections of the brain were performed. One section was stained with haematoxylin and eosin, and four sections were used for immunohistochemistry and labelled with antibodies against calbindin (ab229915; lot no. GR3361538-6; Abcam) for targeting Purkinje cells, myelin basic protein (ab218011; lot no. 1007654-30; Abcam) for targeting myelin sheaths, IBA1 (ab178846; lot no. 1002201-50; Abcam) for targeting microglia and macrophages and glial fibrillary acidic protein (ab7260; lot no. GR3454901-1; Abcam) for targeting astrocytes. Immunohistochemistry was performed using a BOND-III (Leica Biosystems).

Histopathological evaluation

Histopathological evaluation was performed by an EBVS European Veterinary Specialist in Pathology using an Olympus BX46 microscope. Illustrative microscopic images were captured with an Olympus SC50 camera. Evaluation of the CNS was performed independently in the following neuroanatomical locations: cerebellum, hindbrain (pons and medulla), midbrain, interbrain (thalamus and hypothalamus), basal ganglia (striatum and pallidum), hippocampus, isocortex (somatomotor, somatosensory and visual areas) and olfactory bulb. Histological changes were described according to distribution, severity and morphological characteristics. Severity scores were assigned on a scale of 1–5 as follows: grade 1, minimal; grade 2, slight; grade 3, moderate; grade 4, marked; grade 5, severe. Histopathological findings recorded in different neuroanatomical locations of the CNS included the following: Purkinje cell loss (decreased number of soma/decreased dendrites), microgliosis (increased number/activation of microglia), astrocytosis (increased number/activation of astrocytes), demyelination and foam cell formation. After independent evaluation of the aforementioned neuroanatomical regions, the mean severity score for each finding throughout the CNS was calculated. Histopathological findings in other organs included the following: hyperplasia of Kupffer cells (increased number/activation/foamy cytoplasm) and vacuolation of hepatocytes (cytoplasmic alteration/glycogen/lipid accumulation) in the livers, hyperplasia of histiocytes (increased number/activation/foamy cytoplasm) and atrophy of lymphocytes (decreased number in the white pulp) in the spleens, and alveolar macrophages (activated/foamy cytoplasm) and cell debris in the alveolar lumen of the lungs.

Histomorphometry

Histomorphometric analyses were performed on calbindin-immunolabelled CNS sections in all the animals to quantify the number of Purkinje cells. Slides were scanned using an Olympus Slideview VS200 slide scanner coupled to an Olympus VS-264C camera using a $\times 40$ objective to obtain whole slide images (WSIs). Histomorphometric evaluation was conducted in QuPath⁵⁶, quantitative pathology and bioimage analysis software, v.0.4.3. The cerebellum was annotated as the region of interest (ROI). A cell detection algorithm was used to detect the soma of calbindin-positive cells (that is, Purkinje cells).

Cell culture

HEK293T cells (American Type Culture Collection CRL-3216), HeLa cells (American Type Culture Collection CRM-CCL2) and their derivatives were cultured in Dulbecco's modified Eagle's medium (DMEM; Gibco) supplemented with 10% heat-inactivated fetal bovine serum (FBS) (Thermo Fisher Scientific) with 2 mM glutamine, 100 IU ml⁻¹ penicillin and 100 μ g ml⁻¹ streptomycin (Thermo Fisher Scientific). HEK293T cells were authenticated using short tandem repeat profiling. The cell cultures were maintained at 37 °C in an incubator with 5% CO₂. PLA2G15-deficient clone1 cells with LysoTag were obtained from a previous study⁷. For protein expression, Expi293F cells (Thermo Fisher Scientific) were maintained in a shaking incubator at 37 °C with 8% CO₂. These cells were routinely tested for mycoplasma contamination.

Generation of knockout cell lines using CRISPR–Cas9 technology

PLA2G15 knockout clone1 cells have been described previously⁷. PLA2G15 knockout HEK293T clone2 and clone3 and HeLa cells were generated following the Synthego Gene Knockout Kit v.2 protocol using the following mixed guide sgRNA sequences: GGGGCGGAGG UGGAGGCCA; UUAGCAGCAGCAAGAGGAAC and CCUCACCCAGC ACCACUGGG.

In short, a combined 180-pmol sgRNA and 20-pmol Cas9 (Integrated DNA Technologies) was incubated at room temperature for 10 min. Concurrently, HEK293Ts were washed with PBS, detached using enzyme-free dissociation buffer (Thermo Fisher Scientific) and counted

to determine their density. A suspension of 150,000 cells was added to the newly formed ribonucleoprotein complexes, transferred to a Lonza Nucleocuvette and electroporated using the CM-130 program code. Following electroporation, the cells were placed in growth medium and transferred to a 24-well plate. Single-cell populations were obtained using limited dilution, and the sgRNA target sites were sequenced after PCR amplification. Finally, genetic knockouts were confirmed using Synthego ICE CRISPR analysis, an insertion and deletion deconvolution web-based tool (<https://synthego.com>).

Cell volume measurement

Beckman Z2 particle counter and size analyser was used to determine cell count and volume. The filtering criteria were configured to select cells between 10 and 30 μ m in size.

Lysosomal immunopurification from mouse tissues and HEK293Ts

Lysosomes were purified from the brains and livers of mice and HEK293T cells, following established protocols^{14,17}. The brains of mice were obtained after euthanasia. Small uniform liver samples were collected using a 4-mm-diameter biopsy punch to minimize variability between samples. Both brain and liver tissues were used immediately without freezing using the steps described in the lysosomal immunopurification (LysoIP) protocols^{14,17}. During the lysosomal lysate enzyme assays, whole brain or liver tissue was sectioned into three pieces and dounced 30 times with 3-ml PBS supplemented with protease inhibitor. The resulting lysates were centrifuged at 1,000g at 4 °C for 10 min. The supernatant was then transferred to a 15-ml Falcon tube containing 0.5-ml anti-haemagglutinin beads and incubated at 4 °C for 1 h with rotational mixing. Subsequently, the mixture was thoroughly washed and isolated to obtain protein fractions suitable for lysosomal lysate experiments, as previously described⁷. Before enzymatic assays were performed, the protein concentrations in the lysates were quantified using a Pierce BCA Protein Assay Kit (Thermo Fisher Scientific). For cell-based assay, an equal number of cells were cultured and allowed to reach at least 80% confluence before each LysoIP. The homogenization and LysoIP from HEK293Ts were adapted from a previous study¹⁴ and (<https://doi.org/10.17504/protocols.io.bybjpskn>).

Expression and purification of proteins

Expi293F cells were cultured using a combination of two-thirds FreeStyle 293 and one-third Expi293 media and transfected with the PLA2G15 plasmids at a density of 3E6 cells ml⁻¹. Using FectoPRO transfection reagent (Polyplus), transfection was performed at a ratio of 1.3- μ l FectoPRO to 0.5- μ g plasmid DNA per millilitre of cells. Following transfection, glucose and valproic acid were added immediately to reach the final concentrations of 0.4% glucose (w/v) and 0.05% valproic acid (w/v). Equivalent amounts of valproic acid and glucose were added 1 day after transfection, and cells were harvested 3 days after transfection. The culture medium was harvested and combined with PBS in a 1:1 ratio. HisPur Ni-NTA resin was added to the mixture and incubated at 4 °C for 16 h. The resin was washed four times consecutively using different wash compositions before being packed onto a column. The first wash included 50 mM HEPES (pH 7.25), 500 mM NaCl, 0.1 mM EDTA, 5 mM β -mercaptoethanol, 1 mM dithiothreitol, 1 mM phenylmethylsulfonyl fluoride, 20 mM imidazole (pH 7.25), cComplete EDTA-free protease inhibitor cocktail (Roche), 5% glycerol (v/v) and 1% Triton X-100 (v/v). The second wash was identical to the first wash, except for the addition of 10 mM imidazole (pH 7.25) and the absence of Triton X-100 and protease inhibitor. Imidazole was absent from the third wash, which was identical to the second wash except that it contained 250 mM NaCl. The fourth wash was identical to the third wash, except for the addition of 125 mM NaCl. Buffer containing 300 mM imidazole (pH 7.25), 50 mM HEPES (pH 7.25), 125 mM NaCl, 5% glycerol (v/v), 5 mM β -mercaptoethanol, 1 mM dithiothreitol, 0.1 mM EDTA, 1 mM phenylmethylsulfonyl fluoride and protease inhibitors was used

Article

to elute the protein. Using an Amicon 10-kDa MWCO concentrator, the eluted protein was concentrated and further purified by size exclusion chromatography on a Superdex 200 10/300 column. The fractions were then combined, concentrated using an Amicon 10-kDa MWCO concentrator to achieve a final protein concentration of 1 mg ml⁻¹ and swiftly frozen in liquid nitrogen.

Preparation of liposomes

Unless otherwise specified, 18:1 Diether PC (Avanti) was used to make lipid liposomes. The lipids were dried and combined in a tube with 2-ml water and 3-ml diisopropyl ether to create liposomes that contained only glycerophospholipids. The resulting mixture was sonicated for 10 min in a water bath to create tiny unilamellar vesicles, which were subsequently dried. Dried liposomes were resuspended in water, and Stewart assay was used to determine their concentration.

Enzyme assays

Recombinant PLA2G15-6xHis at 100 nM concentration was mixed with phospholipid substrates (BMP or phosphatidylglycerol isomers) of varying concentrations in 50 mM sodium acetate:acetic acid at pH 4.5 and 150 mM NaCl. Liposomes containing phospholipids had an 18:1 Diether PC that was non-cleavable. All lipids and their catalogue numbers are provided in Supplementary Table 10. The 2,2',*R,R* BMP and 2,2',*S,S* BMP compounds were obtained from WuXi AppTec. The mixture was incubated at 37 °C for 30 s to monitor products and for 10 min to monitor substrates, followed by heat inactivation at 95 °C for 5 min. To adjust for background in each experiment, controls containing all components except the enzyme were prepared for each substrate. A time course was carried out at various substrate concentrations to guarantee the linearity of the velocity. The reaction mixture was transferred to plastic autosampler vials to monitor GPG release. For BMP or LPG monitoring, lipids were extracted as described below and transferred to glass autosampler vials. For kinetic studies, the corresponding standard for GPG, LPG or BMP was measured at increasing concentrations to extrapolate the concentrations of the products. For time-dependent BMP isomer comparison, 100 nM recombinant wild-type PLA2G15-6xHis was mixed with 20 μM BMP substrates in 50 mM sodium acetate:acetic acid at pH 4.5 and 150 mM NaCl. The optimum pH was determined using buffers containing sodium acetate:acetic acid, HEPES and boric acid in their respective pH ranges.

Enzyme activity assays in lysosomal protein extract

Lysosomes obtained from mouse tissues or HEK293T cells were lysed using hypotonic water for 1 h to release the soluble lysosomal proteins. The lysosomal protein extract was then combined with 1 μM 3,3',*S,S* BMP and incubated at 37 °C in 50 mM sodium acetate:acetic acid (pH 5) and 150 mM NaCl for the indicated time points. The reaction was stopped using a chloroform:methanol solution in a ratio of 2:1 (v/v) for lipids or 80% methanol for polar metabolite measurements.

Inhibition assays

For inhibition assays, each inhibitor was preincubated with the substrates before either purified PLA2G15-6xHis or lysosomal lysate was added. The reaction buffer contained 50 mM sodium acetate:acetic acid (pH 5.0) and 150 mM NaCl, and we followed the enzyme assays described earlier.

Pulse-chase experiments

A 10× concentration of BMP isomers at a concentration of 100 μM in ethanol, along with fatty acid-free bovine serum albumin (BSA) at the same concentration in PBS, was initially prepared. The concentrated solution was then diluted to a final concentration of 1× in DMEM (Thermo Fisher Scientific). *CLN5* PLA2G15 double-knockout cells were seeded into each well of a poly-L-lysine-coated six-well plate. The next day, the medium was gently aspirated, replaced with serum-free DMEM containing 1×

solution of BSA-conjugated BMP and incubated for 2 h. After incubation, the cells were washed once with serum-free medium and replaced with complete DMEM-containing vehicle solution (1× PBS), 150 nM wild-type PLA2G15-6xHis or 150 nM PLA2G15(S198A) mutant to chase BMP degradation at varying times. Subsequently, both treated and untreated cells were collected in 200 μl of 80% methanol. Lipids were extracted using a two-phase extraction method involving a 2:1 chloroform:methanol (v/v) mixture, as described below. Finally, lipids were analysed with LC-MS.

Enzyme supplementation

To validate the lysosomal localization of the recombinant enzymes, PLA2G15-6xHis and the mutant were labelled with NHS Alexa 488 dye (Thermo Fisher Scientific) according to the manufacturer's protocol. Afterwards, 50,000 PLA2G15 knockout or *CLN5* PLA2G15 double-knockout cells were seeded with 700-μl DMEM medium on each division of a four-chamber 35-mm glass bottom dish (Cellvis). The cells were then treated with 50 nM fluorescently labelled protein in complete medium for 2 days. After a 2-day incubation, the medium was replaced with 700 μl of DMEM containing 1 μM LysoTracker Red DND-99 (Thermo Fisher Scientific) and 1 μg ml⁻¹ of Hoechst 33342 and then incubated for an extra 30 min. The medium was then replaced with fresh medium and immediately imaged with a Leica LSM 980 ZEN confocal microscope ZEN 3.6 (blue edition). The images were analysed using ImageJ v.2.1.0 and CellProfiler v.4.2.7.

For enzyme supplementation experiments, 600,000 cells were seeded into a six-well plate. After 24 h, the cells were treated with 50 nM PLA2G15 wild-type and mutant proteins in complete medium. After 48 h, lipids were extracted as described above and analysed using lipidomics.

Lipid and polar metabolite extraction

Samples were processed for lipid or polar metabolite extraction, following a previous protocol¹⁷. For lipid extraction, 950 μl of 2:1 (v/v) chloroform:methanol containing SPLASH LIPIDOMIX internal standard mix at a concentration of 750 ng ml⁻¹ was added to all the samples. The mixture was then vortexed for 1 h at 4 °C. Subsequently, 200 μl of 0.9% (w/v) NaCl was added, and the mixture was vortexed for 10 min at 4 °C. The mixture was spun at 3,000g for 15 min at 4 °C. The lower chloroform phase, which contained lipids, was collected and dried using a SpeedVac. The dried lipid extracts were reconstituted in 50 μl of 13:6:1 (v/v/v) acetonitrile:isopropyl alcohol:water and vortexed for 10 min at 4 °C in a cold room. The samples were then centrifuged at maximum speed for 10 min at 4 °C, and 45 μl was transferred into glass vials with inserts for LC-MS analysis. For GPG analysis, samples were extracted using 80% methanol in LC-MS grade water containing 500 nM isotope-labelled amino acids as internal standards (Cambridge Isotope Laboratories). The samples were then vortexed for 10 min at 4 °C, centrifuged at 20,627g and transferred into polar vials for LC-MS.

Untargeted lipidomic analysis

Lipidomic analysis of the samples listed in Extended Data Fig. 9h,i and Supplementary Table 8 was performed at the Core Facility Metabolomics of the Amsterdam UMC. In a 2-ml tube, the following amounts of internal standards dissolved in 1:1 (v/v) methanol:chloroform were added to each sample: BMP(14:0/14:0) (0.2 nmol), ceramide-1-phosphate C1P(d18:1/12:0) (0.125 nmol), D7-cholesteryl ester CE(16:0) (2.5 nmol), ceramide Cer(d18:1/12:0) (0.125 nmol), ceramide Cer(d18:1/25:0) (0.125 nmol), cardiolipin CL(14:0/14:0/14:0/14:0) (0.1 nmol), diacylglycerol DG(14:0/14:0) (0.5 nmol), glucosylceramide GlcCer(d18:1/12:0) (0.125 nmol), lactosylceramide LacCer(d18:1/12:0) (0.125 nmol), lysophosphatidic acid LPA(14:0) (0.1 nmol), lysophosphatidylcholine LPC(14:0) (0.5 nmol), lysophosphatidylethanolamine LPE(14:0) (0.1 nmol), lysophosphatidylglycerol LPG(14:0) (0.02 nmol), phosphatidic acid PA(14:0/14:0) (0.5 nmol), phosphatidylcholine PC(14:0/14:0) (2 nmol), phosphatidylethanolamine PE(14:0/14:0) (0.5 nmol), phosphatidylglycerol PG(14:0/14:0)

(0.1 nmol), phosphatidylinositol PI(8:0/8:0) (0.5 nmol), phosphatidylserine PS(14:0/14:0) (5 nmol), sphinganine-1-phosphate SIP(d17:0) (0.125 nmol), sphinganine-1-phosphate SIP(d17:1) (0.125 nmol), ceramide phosphocholines SM(d18:1/12:0) (2.125 nmol), sphingosine SPH(d17:0) (0.125 nmol), sphingosine SPH(d17:1) (0.125 nmol) and triacylglycerol TAG(14:0)₂ (0.5 nmol). All internal standards were purchased from Avanti Polar Lipids. After addition of the internal standards, 1.5 ml 1:1 (v/v) methanol:chloroform was added before thorough mixing. The samples were then centrifuged for 10 min at 14,000 rpm, and the supernatant was transferred to a glass vial and evaporated under a stream of nitrogen at 60 °C. The residue was dissolved in 150 µl of 1:1 (v/v) methanol:chloroform. Lipids were analysed using an Ultimate 3000 binary HPLC coupled to a Q Exactive Plus Orbitrap mass spectrometer (Thermo Fisher Scientific). For normal phase separation, 5 µl of each sample was injected onto a Phenomenex Luna Silica, 250 × 2 mm, 5 µm 100 Å. The column temperature was held at 25 °C. The mobile phase consisted of 85:15 (v/v) methanol:water containing 0.0125% formic acid and 3.35 mmol l⁻¹ of ammonia (A) and 97:3 (v/v) chloroform:methanol containing 0.0125% formic acid (B). Using a flow rate of 0.3 ml min⁻¹, the liquid chromatography gradient consisted of isocratic at 10% A 0–1 min, ramp to 20% A at 4 min, ramp to 85% A at 12 min, ramp to 100% A at 12.1 min, isocratic at 100% A at 12.1–14 min, ramp to 10% A at 14.1 min and isocratic at 10% A for 14.1–15 min. For reversed phase separation, 5 µl of each sample was injected onto a Waters HSS T3 column (150 × 2.1 mm; 1.8-µm particle size). The column temperature was held at 60 °C. The mobile phase consisted of 4:6 (v/v) methanol:water (A) and 1:9 (v/v) methanol:isopropanol (B), both containing 0.1% formic acid and 10 mmol l⁻¹ of ammonia. Using a flow rate of 0.4 ml min⁻¹, the liquid chromatography gradient consisted of isocratic at 100% A at 0 min, ramp to 80% A at 1 min, ramp to 0% A at 16 min, isocratic at 0% A for 16–20 min, ramp to 100% A at 20.1 min and isocratic at 100% A for 20.1–21 min. Mass spectrometry data were acquired using negative and positive ionization by continuous scanning over the range of *m/z* 150–2,000 at a resolution of 280,000 full-width at half-maximum. Data were analysed using an in-house developed lipidomics pipeline written in the R programming language (<http://www.r-project.org>) and MATLAB⁵⁷. Lipid identification was on the basis of a combination of accurate mass, (relative) retention times, fragmentation spectra (when required), analysis of samples with known metabolic defects and the injection of relevant standards. Lipid classes were defined in our lipidomics pipeline in terms of their generic chemical formula, where *R* represents the radical group. Upon import of the lipid database into the annotation pipeline, the generic chemical formula of each lipid class is expanded by replacing the *R* element with a range of possible radical group lengths and double bond numbers. The resulting expanded list of chemical formulas was used to calculate the neutral monoisotopic mass of each species. The reported lipid abundances are semiquantitative and calculated by dividing the response of the analyte (area of the peak) by that of the corresponding internal standard multiplied by the concentration of the internal standard (a.u.). The suffix [O] indicates lipids containing an alkyl-ether group, whereas the addition of a quote ' indicates an alkenyl-ether group. As no dedicated internal standard for ether lipids is available, we used the lysophosphatidylcholine, phosphatidylcholine, lysophosphatidylethanolamine and phosphatidylethanolamine internal standards to normalize the corresponding ether lipid species, as described above.

Targeted lipidomics and polar metabolomics

Targeted analyses were adapted and performed, as previously described^{3,7,31}. Lipids were separated on an Agilent RRHD Eclipse Plus C18, 2.1 × 100 mm, 1.8u-BC column with an Agilent guard holder (UHPLC Grd; Ecl. Plus C18; 2.1 mm; 1.8 µm), whereas polar metabolites were separated using hydrophilic interaction chromatography using a SeQuant ZIC-pHILIC 50 × 2.1 mm column (MilliporeSigma 1504590001) with a 20 × 2.1 mm (MilliporeSigma 1504380001) guard. Before mass

spectrometry, the columns were connected to a 1290 LC system for lipid and metabolite separation. The liquid chromatography system was linked to an Ultivo triple quadrupole (QQQ) mass spectrometer with a liquid chromatography–electrospray ionization probe. External mass calibration was performed weekly using a QQQ standard tuning mix. The column compressor and autosampler were held at 45 °C and 4 °C, respectively. For lipidomics, the mass spectrometer parameters included a capillary voltage of 4.4 kV in positive mode and 5.5 kV in negative mode, and the gas temperature and sheath gas flow were held at 200 °C and 275 °C, respectively. The gas flow and sheath gas flow were 10 and 11 l min⁻¹, respectively, whereas the nebulizer was maintained at 45 psi. The nozzle voltages were maintained at 500 in the positive mode and 1,000 in the negative mode. These conditions were held constant for both ionization mode acquisition. For metabolomics, similar conditions were used, except for the gas temperature and sheath gas flow, which were held at 250 °C and 300 °C, respectively. Additionally, the gas flow and nebulizer pressure were 13 l min⁻¹ and 30 psi.

For lipid measurements, 2- to 4-µl injection volumes were used for each sample for polarity switching. A mobile phase with two distinct components (A and B) was used in the chromatographic process. Mobile phase A was a mixture of acetonitrile:water (2:3 (v/v)), whereas mobile phase B was composed of isopropanol:acetonitrile (9:1 (v/v)), both containing 0.1% formic acid and 10 mM ammonium formate. The elution gradient was carried out over a total of 16 min, with an isocratic elution of 15% B for the first minute, followed by a gradual increase to 70% of B over 3 min and then to 100% of B from 3 to 14 min. Subsequently, this was maintained from 14 to 15 min, after which solvent B was reduced to 15% and maintained for 1 min, followed by an extra 2 min for column re-equilibration. The flow rate was set to 0.400 ml min⁻¹.

For polar metabolite measurements, each sample was injected with a volume of 1–2.5 µl. Mobile phase A was composed of 20 mM ammonium carbonate and 0.1% ammonium hydroxide dissolved in LC–MS grade water, whereas mobile phase B was composed of 100% LC–MS grade acetonitrile. Elution was performed over a 10-min gradient; the B component was linearly decreased from 80% to 20% between 0 and 7 min, rapidly increased from 20% to 80% between 7 and 7.5 min and was held at 80% B from 7.5 to 10 min. The flow rate was set to 0.15 ml min⁻¹.

The QQQ was set to operate in multiple reaction monitoring (MRM) to analyse compounds of interest. Standard lipids, glycerophosphodiesters and amino acids were optimized using the MassHunter Optimizer MRM, a software used for automated method development. For most species, the two most abundant transitions were selected to detect it. The precursor–product ion pairs (*m/z*) of the compounds used for MRM are listed in Supplementary Table 10.

Polar metabolites and lipids were annotated, and their abundances were measured using the Qualitative MassHunter acquisition software and QQQ quantitative analysis software (Quant My-Way), respectively. The peak areas of all metabolites were integrated using the retention time and MRM method, and the resulting raw abundances were exported to Microsoft Excel for further analysis. The raw abundances of internal controls, endogenous amino acids and highly abundant lipids were examined to ensure the accuracy of the analysis. Raw abundances were normalized to cell numbers using the abundance of endogenous control lipids in the same sample. Quality control samples were consistently measured to ensure optimal instrument performance and linearity. The average of the blank samples was subtracted from all raw abundances. For fold-change calculations, each sample was divided by the average of wild-type or control samples. For total BMP calculations, the sum of all abundances of the measured BMPs was used to generate these values.

Cholesterol measurement

Cholesterol was detected in the left hemibrains and left liver lobes of four animals per group (three samples each from each animal) using

Article

a commercial kit (ab65359; Abcam). Left hemibrains and left liver lobes were homogenized in 4 (v/w) PBS using a UPHO bead mill (GENE-EYE; SOP NEQU200) at 60 Hz for 55 s. Then, 100 μ l of the homogenate was transferred to a fresh Eppendorf tube for further processing, and a 5- μ l aliquot was used for total protein determination (Pierce BCA assay; Thermo Fisher Scientific; 23225). For extraction, 200 μ l of chloroform:isopropanol:NP-40 (7:11:0.1) was added to a 100- μ l aliquot, and the sample was vortexed vigorously two times after 5–10 min of incubation phase in between. The extract was then centrifuged for 5–10 min at 15,000g. The entire chloroform phase was transferred to a new tube and air-dried at 50 °C for up to 24 h. The dried lipids were dissolved by vortexing with 100 μ l of Assay Buffer II (from kit ab65359) and stored at –80 °C until further use. Cholesterol was assessed in parallel in all samples following the protocol of the commercially available Cholesterol/Cholesteryl Ester Quantitation Assay Kit (ab65359). Fluorescence was measured using a microplate reader (Cytation 5; SOP NEQU201) at excitation/emission = 535/587 nm.

Immunoblotting

Purified proteins were run on SDS–PAGE (Thermo Fisher Scientific) at 120 V and transferred to polyvinylidene difluoride membranes at 40 V for 2 h. The membranes were then blocked with 5% non-fat dry milk in Tris-buffered saline with 0.1% Tween 20 (TBST) for 30 min and incubated overnight with primary antibodies in 5% BSA in TBST at 4 °C using dilutions listed in the antibody table. After incubation, the membranes were washed three times with TBST for 5 min per wash and then incubated with appropriate secondary antibodies diluted 1:3,000 in 5% BSA for 1 h at room temperature. Membranes were then washed three times with TBST followed by ECL2 western blotting substrate (Thermo Fisher Scientific) before visualization.

Thermal stability assay

A Tycho NT.6 instrument (NanoTemper Technologies) was used to determine the melting stability of human wild-type PLA2G15-6xHis and S198A. Purified proteins (5 μ M) in 50 mM sodium acetate–acetic acid (pH 5.0) and 150 mM NaCl were loaded into Tycho NT.6 capillaries. The melting temperature (T_m) was obtained by plotting the absorbance ratio of solvent-exposed tryptophan versus buried tryptophan (350 nm/330 nm) over a temperature gradient and determining the inflection temperature from the first derivative.

Microscale thermophoresis

Recombinant human PLA2G15-6xHis S198A was labelled using a RED-NHS Protein Labeling Kit, following the manufacturer's protocol. A Monolith NT.115 instrument was used for binding experiments. A 100 nM labelled protein was incubated with serial dilutions of substrates in 50 mM sodium acetate–acetic acid (pH 5.0), 150 mM NaCl and 5 μ M BSA for 30 min at room temperature. Using premium capillaries, binding measurements were conducted at 20%, 40% or 60% microscale thermophoresis power for 30 s with 5 s of cooling. The dissociation constant K_d was derived by plotting the fraction bound against logarithmic substrate concentrations according to the law of mass action.

Synthesis of GPG

Standard GPG was prepared for kinetic assays. Phosphatidylglycerol (18:1/18:1; Avanti) was saponified to produce GPG according to the following protocol: 100 mg of phosphatidylglycerol was dissolved in a 20-ml scintillation vial that contained a 12-ml solution of 2:1 chloroform:methanol with a magnetic stirring bar. NaOH (2 M; 4 ml) was added to the mixture, and the reaction was stirred for 2 h at room temperature. To neutralize the reaction, 2 M HCl (4 ml) was used, and GPG was extracted with 8-ml water into separate vessels twice. After mixing the aqueous phases, they were frozen in liquid nitrogen, lyophilized and cleaned with 8 ml of chloroform. To separate the crude product from the inorganic salts, lyophilates were dissolved in a minimal

amount of methanol. The desired products were then extracted from the precipitate using filter paper.

Thin-layer chromatography

Wild-type PLA2G15-6xHis (100 nM) was mixed with 20 μ M BMP and incubated at 37 °C for 1 h, as described for the enzyme assay. Two microlitres of the reaction mixture was spotted on silica and optimized to observe product release. The silica was placed in a thin-layer chromatography solvent ($\text{CHCl}_3/\text{CH}_3\text{OH}/\text{concentrated ammonia}/\text{water}$ (90:54:5.5:2 (v/v))) and dipped into an iodine stain (iodine crystals and silica gel mixture) after the solvent run before visualization.

DiffDock docking

The structure of *Homo sapiens* PLA2G15 was obtained from the AlphaFold entry Q8NCC3 (UniProt). The predicted protein structure was prepared for docking using ChimeraX to add hydrogen according to the expected protonation state at pH 5. The substrates were drawn in ChemDraw to extract the SMILES string. The structure of the protein (Protein Data Bank format) and the SMILES string were used as inputs for DiffDock. DiffDock was run on a web server using the following parameters: 20 inference steps, 18 actual inference steps and 40 samples. The docking results with the best confidence scores were used for analysis using ChimeraX.

siRNA knockdown in mouse BMDMs

A total of 100,000 BMDMs isolated from *Gba*^{+/+} or *Gba*^{+/D409V} mice were seeded into each well on each division of a four-chamber 35-mm glass bottom dish (Cellvis) that contains 750- μ l complete DMEM. The next day, the cells were transfected with scramble siRNA (Thermo Fisher Scientific; 4390844) or two siRNAs targeting mouse PLA2G15 (Thermo Fisher Scientific; si101347 and si101348) using RNAiMAX (Thermo Fisher Scientific) according to the manufacturer's instructions. Three days after transfection, the cells were subjected to the LysoFQ assay, as described below.

LysoFQ–GCase activity assay

About 50,000 bone marrow-derived macrophages were seeded with 700 μ l of macrophage medium on each division of a four-chamber 35-mm glass bottom dish (Cellvis). In the non-siRNA experiment, 300 nM recombinant wild-type or mutant PLA2G15 or vehicle solution (1 \times PBS) was added during cell seeding. After overnight incubation, 10 μ M LysoFQ-GBA probe⁵⁸ was added to the medium and incubated for 30 min. After incubation, the medium was washed once with the macrophage medium and then replaced with fresh medium containing 100 nM AT3375 (GCase inhibitor) to stop the reaction. The cells were then imaged with a Leica LSM980 Zen confocal microscope ZEN 3.6 (blue edition), and images were analysed using ImageJ v.2.1.0.

Haploid genetic screens

To identify regulators of intracellular cholesterol staining, we prepared libraries of mutagenized Hap1 wild-type and NPC1-deficient cells using a gene-trap retrovirus expressing blue fluorescent protein, as previously described⁵⁹. HAP1 cells were acquired under licence from the Whitehead Institute and the Netherlands Cancer Institute and confirmed using genetic analysis. For each genotype, the mutagenized cells were cultured and expanded for 1 week after mutagenesis. Subsequently, the cells were washed with PBS, dissociated, pelleted and fixed with BD Fix Buffer I (BD Biosciences) for 10 min at 37 °C. After washing once with fluorescence-activated cell sorting (FACS) buffer (PBS containing 1% BSA) and once with PBS, the cells were pelleted and resuspended in permeabilization buffer (PBS containing 0.1% saponin). The cells were then incubated for 5 min at room temperature while being continuously rotated. The cells were pelleted, washed twice with FACS buffer and incubated with FACS buffer containing 3 μ g ml^{–1} Alexa Fluor 647-labelled PFO⁶⁰ and 1 μ g ml^{–1} of 4',6-diamidino-2-phenylindole

for 45 min at room temperature while being continuously rotated. The cells were subsequently pelleted and washed twice with FACS buffer before sorting into two populations of cells (PFO-LOW and PFO-HIGH), which represent approximately 5% of the lowest and highest cholesterol-containing cells from the total cell population, respectively. In addition, the cells were sorted in parallel for haploid DNA content (G1 phase) using the 4',6-diamidino-2-phenylindole signal. Cell sorting was carried out on a FACSria III Cell Sorter (BD Biosciences) until approximately ten million cells from each population were collected. The sorted cells were pelleted, and genomic DNA was isolated. The gene-trap insertion sites of each sorted cell population were amplified and mapped by deep sequencing. For each gene in a single screen, a mutation index was calculated corresponding to the ratio of the number of disruptive integrations per gene in both populations normalized by the number of total integrations in each channel (that is, PFO-LOW and PFO-HIGH), as previously described⁵⁹. Genes significantly enriched for disruptive gene-trap integrations in either the PFO-HIGH or PFO-LOW query populations were identified using two-sided Fisher's exact test. The resulting *P* values were adjusted for several testing using the Benjamini–Hochberg false discovery rate correction.

siRNA knockdown in fibroblasts derived from patients with NPC1

Two fibroblast cell lines derived from patients with NPC1 (GM03123 and GM18453) were acquired from Coriell with agreement. From these two fibroblast cell lines, 30,000 cells were seeded in each well of an eight-chamber cell culture slide (CELLTREAT) that contains 500- μ l complete DMEM. The next day, cells were transfected with scrambled siRNA (Thermo Fisher Scientific; 4390844) or two siRNAs targeting human PLA2G15 (Thermo Fisher Scientific; s24296 and s24297) using RNAiMAX (Thermo Fisher Scientific) according to the manufacturer's instruction. Two days after transfection, the medium was gently aspirated, and cells were washed once with 800- μ l PBS, followed by immediate 15-min fixation with 200 μ l of 4% paraformaldehyde in PBS. The cells were then washed once with 800- μ l PBS and stained with 200 μ l of 1 mg ml⁻¹ filipin (Cayman). Slides were sealed with glass coverslips and mounting solution (Thermo Fisher Scientific) and imaged using a Leica LSM980 ZEN confocal microscope ZEN 3.6 (blue edition).

Data preparation and statistics

GraphPad Prism v.10.2 was used for quantitative data presentation, and figures were assembled in Adobe Illustrator 2023. All statistical analyses were performed using Prism software. Unless otherwise stated in the legends, all measurements were derived from independent samples or biological replicates. The Western blot data displayed were representative experiments. ChemDraw v.22.2.0 was used in the chemical structures depicted in Figs. 1a–c, 2a and Extended Data Fig. 5h.

Reporting summary

Further information on research design is available in the Nature Portfolio Reporting Summary linked to this article.

Data availability

All data needed to evaluate the conclusions stated in the paper are presented in the paper and/or the supplementary materials. The original code is not reported in this paper. Cell lines can be requested, and

requests will be fulfilled by the lead author (monther@stanford.edu). All sequencing datasets from the haploid screens were deposited in the National Center for Biotechnology Information Sequence Read Archive under accession number PRJNA1177366. Data from untargeted lipid profiling are available at Zenodo (<https://doi.org/10.5281/zenodo.14170857>)⁶¹. Source data are provided with this paper.

53. Polinski, N. K. et al. Decreased glucocerebrosidase activity and substrate accumulation of glycosphingolipids in a novel GBA1 D409V knock-in mouse model. *PLoS ONE* **16**, e0252325 (2021).
54. Davidson, J. W. et al. Modulation of hepatic transcription factor EB activity during cold exposure uncovers direct regulation of bis(monoacylglycerol)phosphate lipids by *Pla2g15*. Preprint at *bioRxiv* <https://doi.org/10.1101/2023.11.03.565498> (2025).
55. Davidson, C. D. et al. Improved systemic AAV gene therapy with a neurotrophic capsid in Niemann–Pick disease type C1 mice. *Life Sci. Alliance* **4**, e202101040 (2021).
56. Bankhead, P. et al. QuPath: open source software for digital pathology image analysis. *Sci. Rep.* **7**, 16878 (2017).
57. Vaz, F. M. et al. Discovery of novel diagnostic biomarkers for Sjogren–Larsson syndrome by untargeted lipidomics. *Biochim. Biophys. Acta, Mol. Cell. Biol. Lipids* **1869**, 159447 (2024).
58. Deen, M. C. et al. A versatile fluorescence-quenched substrate for quantitative measurement of glucocerebrosidase activity within live cells. *Proc. Natl Acad. Sci. USA* **119**, e2200553119 (2022).
59. Brockmann, M. et al. Genetic wiring maps of single-cell protein states reveal an off-switch for GPCR signalling. *Nature* **546**, 307–311 (2017).
60. Kwiatkowska, K. et al. Visualization of cholesterol deposits in lysosomes of Niemann–Pick type C fibroblasts using recombinant perfringolysin O. *Orphanet J. Rare Dis.* **9**, 64 (2014).
61. Nyame, K., de Jong, A. P. H. & Abu-Remaileh, M. PLA2G15 is a lysosomal BMP hydrolase and its targeting ameliorates lysosomal disease (version 1). *Zenodo* <https://doi.org/10.5281/zenodo.14170857> (2025).

Acknowledgements We thank all the members of the Abu-Remaileh Laboratory and Scenic Biotech for their helpful discussions. We also thank S. Pfeffer for providing microscale thermophoresis, J. A. Shayman for PLA2G15-deficient mouse model and F. Vaz of the Core Facility Metabolomics from UMC Amsterdam for providing untargeted lipid analysis and services. The *Npc1*^{tm1m/J} mouse model work was performed at Scantox. This study was supported by grants from Beatbatten, NCL Foundation (NCL-Stiftung), NIH Director's New Innovator Award Program (1DP2CA271386), Knight Initiative for Brain Resilience, the Innovative Medicines Accelerator at Stanford University and Ara Parseghian Medical Research Foundation to M.A.-R. K.N. is supported by the Sarafan ChEM-H Chemistry/Biology Interface Program as a Kolluri Fellow. K.N. is also supported by the Bio-X Stanford Interdisciplinary Graduate Fellowship affiliated with the Wu Tsai Neurosciences Institute (Bio-X SIGF: Mark and Mary Stevens Interdisciplinary Graduate Fellow). H.N.A. is supported by the Arc Institute Graduate Fellowship Program. I.V.P. is supported by the Chemical Engineering Research Experience for Undergraduates Program. J.A.S. is an HHMI Freeman Hrabowski Scholar and has received grants from the National Institutes of Health, National Institute of Diabetes and Digestive and Kidney Diseases (NIH/NIDDK and R01DK133479). M.A.-R. is a Stanford Terman Fellow and a Pew-Stewart Scholar for Cancer Research, supported by The Pew Charitable Trusts and The Alexander and Margaret Stewart Trust.

Author contributions K.N. and M.A.-R. conceptualized the study. K.N., J.X. and M.A.-R. developed the methodology. K.N., J.X., H.N.A. and I.V.P. conducted the investigation. K.N. performed the mass spectrometry data acquisition and analysis. J.A.S. provided PLA2G15-deficient tissues. R.d.M. conducted the histopathological analysis. M.R., V.A.B., S.M.B.N. and T.R.B. performed genetic modifier screening. M.R., A.P.H.d.J., V.A.B., S.M.B.N., T.R.B. and G.H. coordinated activities related to *Pla2g15* and *Pla2g15/Npc1* mice. M.A.-R. supervised the study. K.N. and M.A.-R. wrote the original draft of this paper. All authors reviewed the paper. M.A.-R. was responsible for funding acquisition.

Competing interests M.A.-R. is a scientific advisory board member of Lycia Therapeutics and senior advisor of Scenic Biotech. M.R., V.A.B., S.M.B.N., T.R.B., A.P.H.d.J. and G.H. are employees or advisors of Scenic Biotech. R.d.M. is an employee of AnaPath Services. The other authors declare no competing interests.

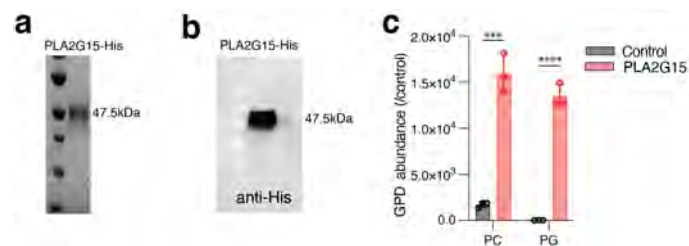
Additional information

Supplementary information The online version contains supplementary material available at <https://doi.org/10.1038/s41586-025-08942-y>.

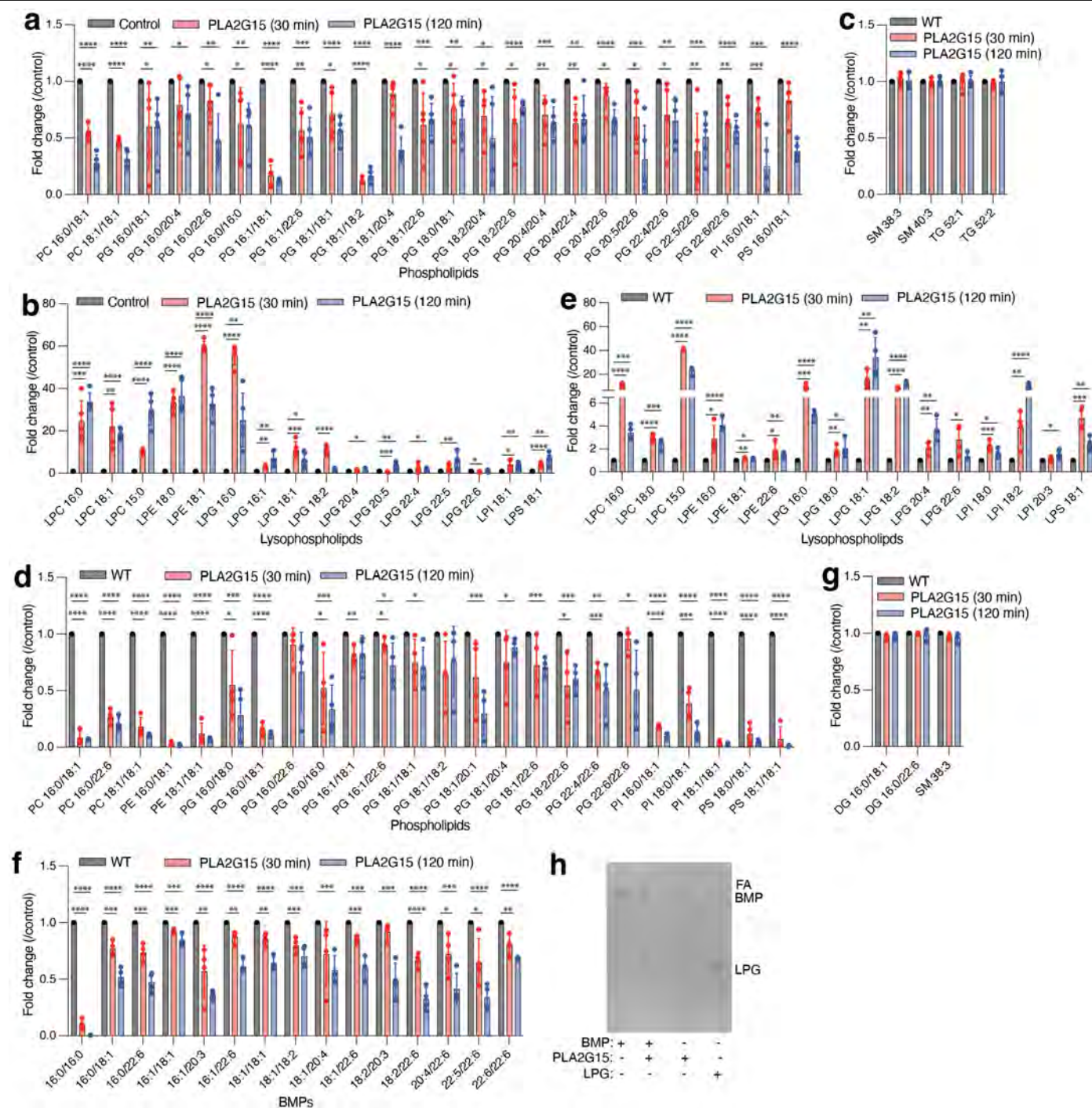
Correspondence and requests for materials should be addressed to Monther Abu-Remaileh.

Peer review information Nature thanks Makoto Murakami, Forbes Porter and the other, anonymous, reviewer(s) for their contribution to the peer review of this work.

Reprints and permissions information is available at <http://www.nature.com/reprints>.

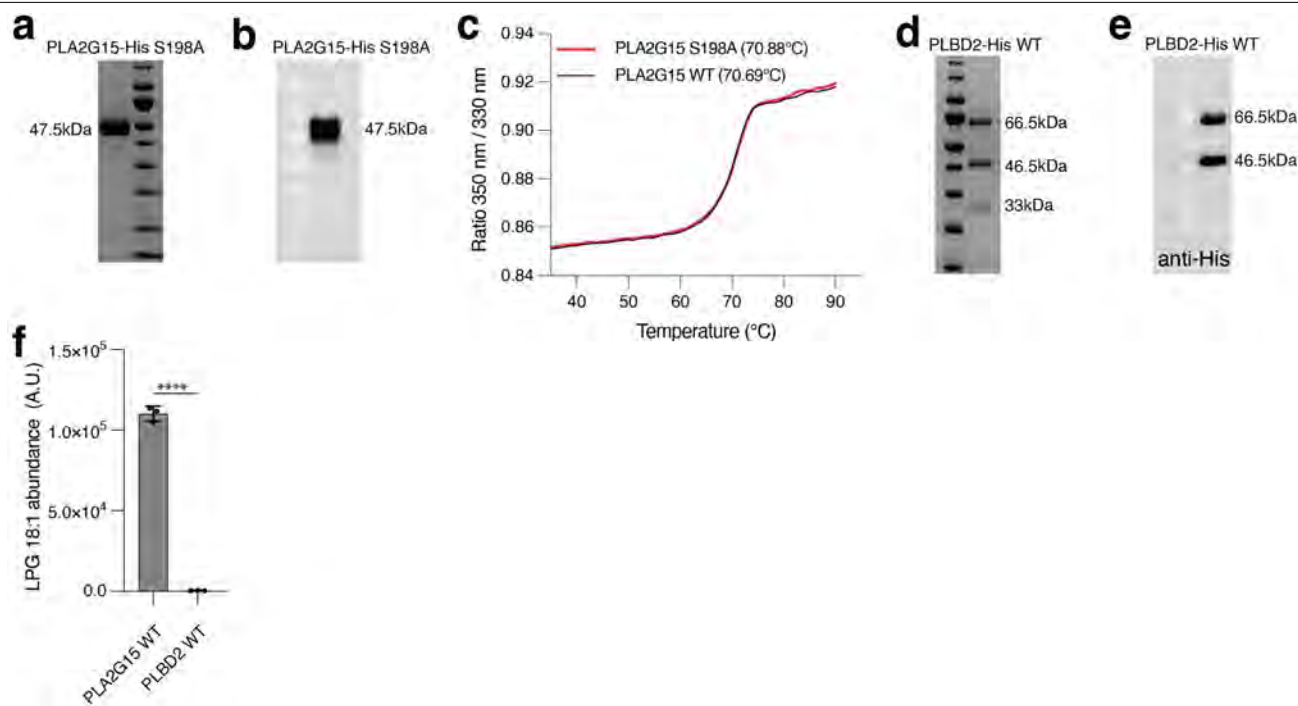


Extended Data Fig. 1 | Purification of recombinant PLA2G15. a, Purification of wildtype recombinant His-tagged lysosomal phospholipase PLA2G15. Representative image of 47.5 kDa PLA2G15-6xHis protein purified to homogeneity and stained with Coomassie Blue. This was repeated at least three times. **b**, Immunoblot analysis of purified PLA2G15 using anti-His antibody. This was repeated at least three times. **c**, Purified PLA2G15 is active enzyme. Phospholipase activity determined using 100 nM PLA2G15 against phosphatidylcholine (PC) or phosphatidylglycerol (PG) under acidic conditions for 1 min. Glycerophosphodiester products (GPD) detected using LC-MS. Data are mean \pm s.d. of $n = 3$ independent replicates for each protein. Statistical analysis was performed using two-tailed unpaired *t*-tests. *** $p = 0.0003$ and **** $p = 0.000051$. Control has all reaction components with no enzyme. Gel source data are provided in Supplementary Fig. 1.



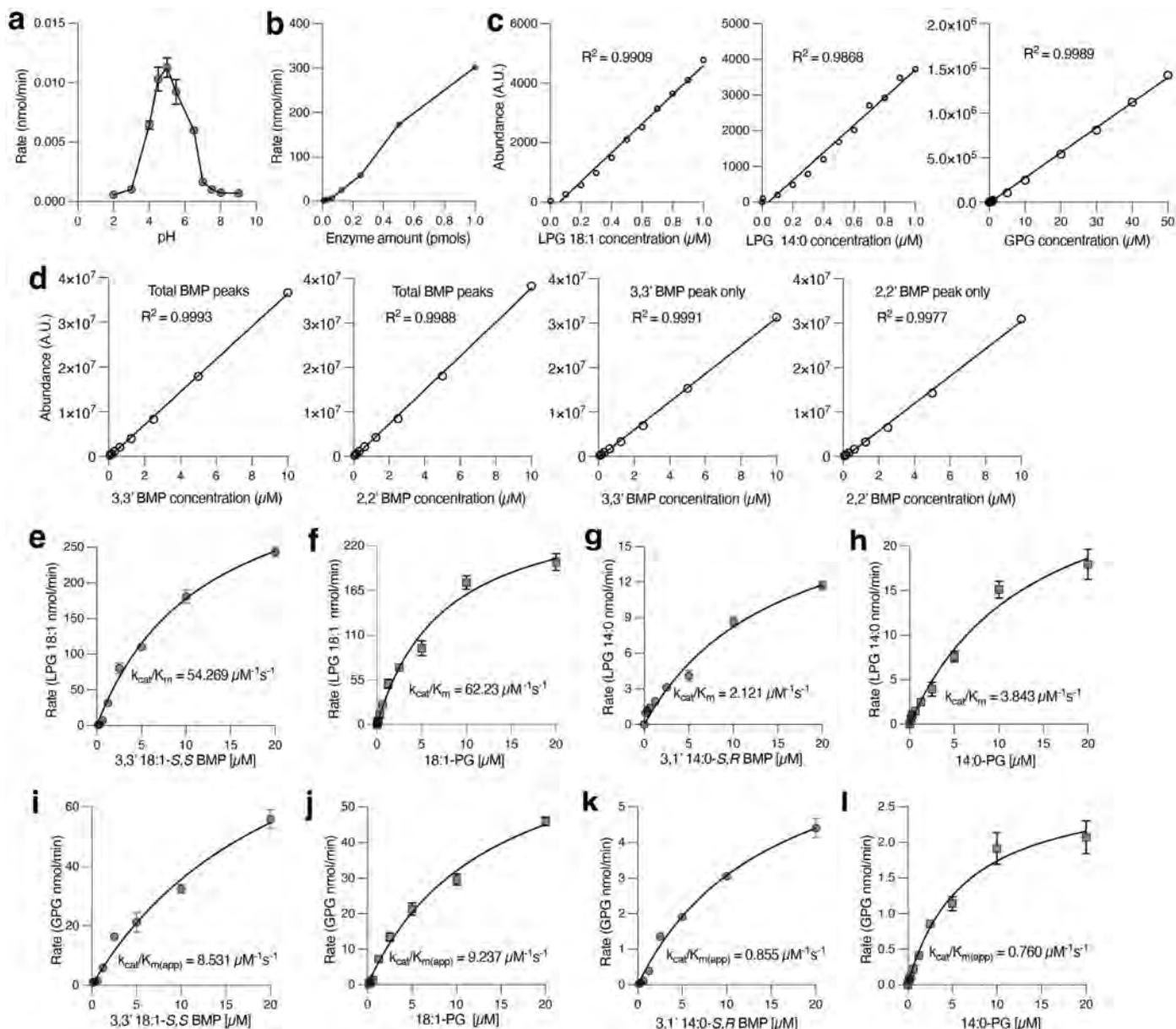
Extended Data Fig. 2 | PLA2G15 catabolizes lysosomal phospholipids including BMP. a,b. PLA2G15 hydrolyzes phospholipid substrates isolated from mouse liver lysosomes. Fold changes in the abundance of known PLA2G15 substrates (PC, PE, PG, PI and PS) in (a) and lysophospholipid intermediates (LPC, LPE, LPG, LPI, LPS) in (b) for 30 min or 120 min reactions. **c.** Non-phospholipids are unchanged in PLA2G15 reaction. Fold changes in sphingomyelin (SM) and triacylglycerol (TG). Each incubation time was compared to control (no enzyme) samples from the same mouse incubated for the same time. Data are mean \pm s.d. of $n = 5$ biological replicates. Statistical analysis was performed using two-tailed unpaired t -tests. * $p < 0.05$, ** $p < 0.01$, *** $p < 0.001$ and **** $p < 0.0001$. **d-f.** PLA2G15 hydrolyzes BMP and other phospholipid substrates extracted from HEK293T lysosomes. Lysosomal lipids were isolated from HEK293T lysosomes and incubated with recombinant PLA2G15 for 30 min or 120 min. Fold changes in phospholipid substrates

(PC, PE, PG, PI and PS) in (d), lysophospholipid intermediates (LPC, LPE, LPG, LPI, LPS) in (e), and BMPs in (f). Data are mean \pm s.d. of $n = 4$ biological replicates. Statistical analysis was performed using two-tailed unpaired t -tests. * $p < 0.05$, ** $p < 0.01$, *** $p < 0.001$ and **** $p < 0.0001$. **g.** Non PLA2G15 substrates remained unchanged. Fold changes in diacylglycerol (DG) and sphingomyelin (SM). Each incubation time was compared to control samples from each biological replicate incubated at the same time. Data are mean \pm s.d. of $n = 4$ biological replicates. **h.** PLA2G15 hydrolyzes synthesized BMP in vitro. Thin Layer Chromatography (see methods) was used to measure the presence of LPG intermediate after incubating wildtype recombinant PLA2G15 with 3,3'-18:1-S,5-BMP under acidic conditions (pH=5.0). Controls had similar reaction buffers except with no enzyme. Putative FA: fatty acid was annotated based on solvent characteristics.



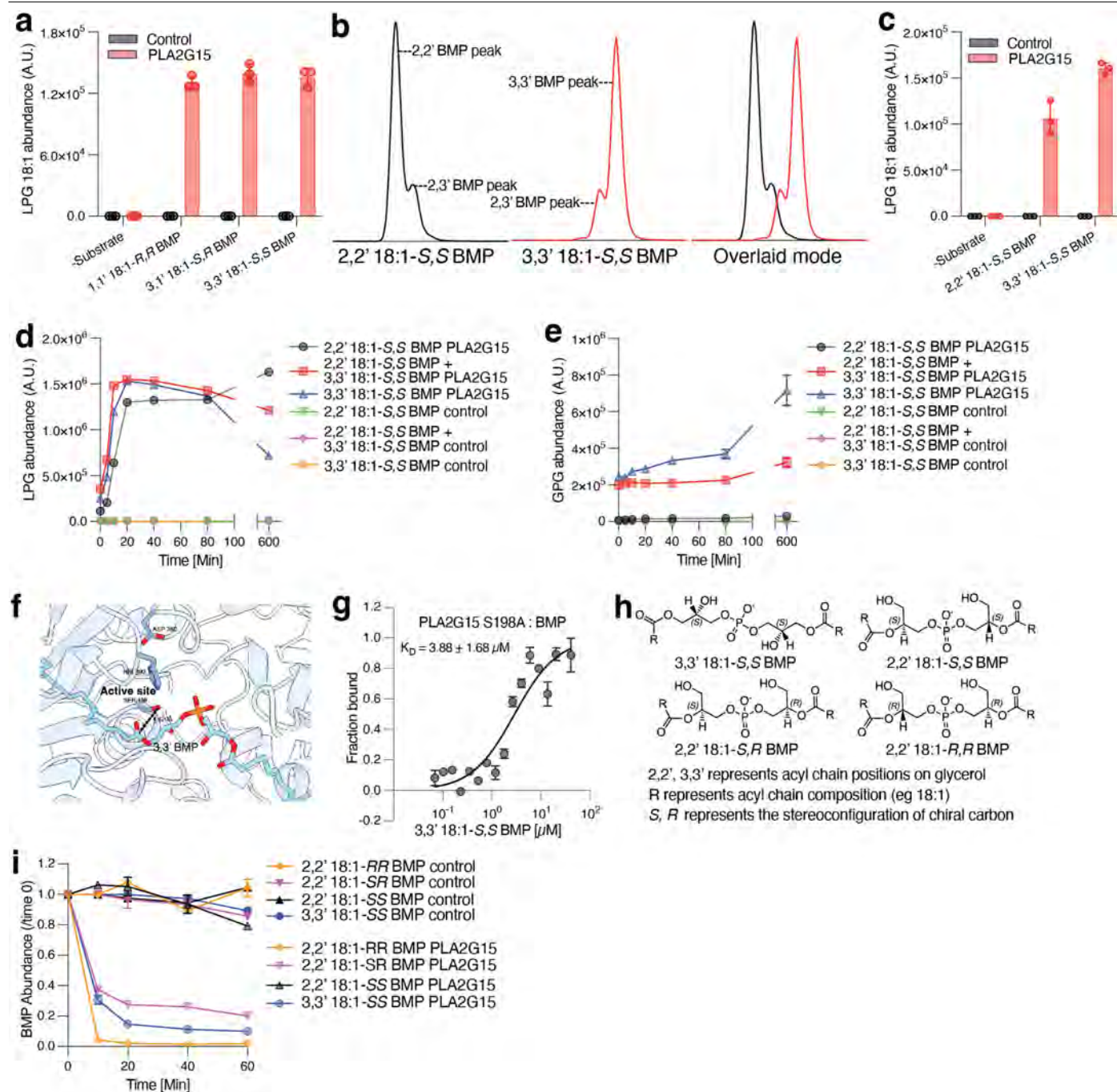
Extended Data Fig. 3 | Purification and characterization of lysosomal phospholipases. **a**, Purification of recombinant His-tagged PLA2G15 S198A. Representative image of 47.5 kDa PLA2G15 S198A-6xHis protein purified to homogeneity and stained with Coomassie Blue. **b**, Immunoblot analysis of PLA2G15 S198A using anti-His antibody. **c**, Melting temperature (T_m) curves indicate that wildtype and S198A mutant maintain thermal stability. T_m is indicated on the graph. **d**, Purification of recombinant His-tagged PLBD2. Representative image of PLBD2-6xHis protein purified to homogeneity and

stained with Coomassie Blue. The three bands are indicative of 66.5 kDa proenzyme, 46.5 kDa matured form and 33 kDa N-terminus pro-domain. **e**, Immunoblot analysis of PLBD2 using anti-His antibody. **f**, PLBD2 has no BMP hydrolase activity. BMP Hydrolase activity by 100 nM wildtype recombinant PLA2G15 and PLBD2 proteins under acidic conditions determined using LC-MS. Data are mean \pm s.d. of $n = 3$ independent replicates from each protein. **** $p = 0.0000021$ using two-tailed unpaired t -tests. Gel source data are provided in Supplementary Fig. 1.



Extended Data Fig. 4 | PLA2G15 has high catalytic activity towards BMP under optimized enzyme reaction conditions. **a**, BMP hydrolase activity of PLA2G15 has an acidic pH optimum. PLA2G15-6xHis was incubated with 3,3' 18:1-S,S BMP under the indicated pH conditions. A representative graph is shown for an experiment repeated at least 3 times. Data are mean \pm s.d. of $n = 3$ independent replicates. **b**, PLA2G15-6xHis was incubated with 1 μ M of 3,3' 18:1-S,S BMP and at different time points and enzyme concentrations. A representative graph indicates linearity in increments across multiple concentrations at a 30 s time point. **c**, Standard curves generated from measuring the indicated LPG and GPG standards. **d**, Standard curves generated from measuring the indicated BMP standards. **e-h**, PLA2G15 deacylates BMP to LPG with high catalytic efficiency that is comparable to that against PG phospholipid and this activity correlates with acyl chain length. Recombinant PLA2G15 was incubated with the indicated phospholipids under acidic conditions (pH = 5.0) for 30 s and

reactions were stopped by heating. Phospholipids were incorporated in liposomes with non-cleavable 18:1 diether PC and indicated LPG intermediates were measured. Each experiment was repeated at least three times, and a representative graph is shown. K_{cat}/K_m is a measure of kinetic efficiency. Data are mean \pm s.d. of $n = 3$ independent replicates. **i-l**, PLA2G15 deacylates BMP to GPG with high efficiency. Recombinant PLA2G15 was incubated with the indicated phospholipids under acidic conditions (pH = 5.0) for 30 s and reactions were stopped by heating. Phospholipids were incorporated in liposomes with non-cleavable 18:1 diether PC and GPG product was measured. Each experiment was repeated at least three times, and a representative graph is shown. "app" is defined as apparent because the catalytic efficiency is derived from a two-step reaction. Data are mean \pm s.d. of $n = 3$ independent replicates.



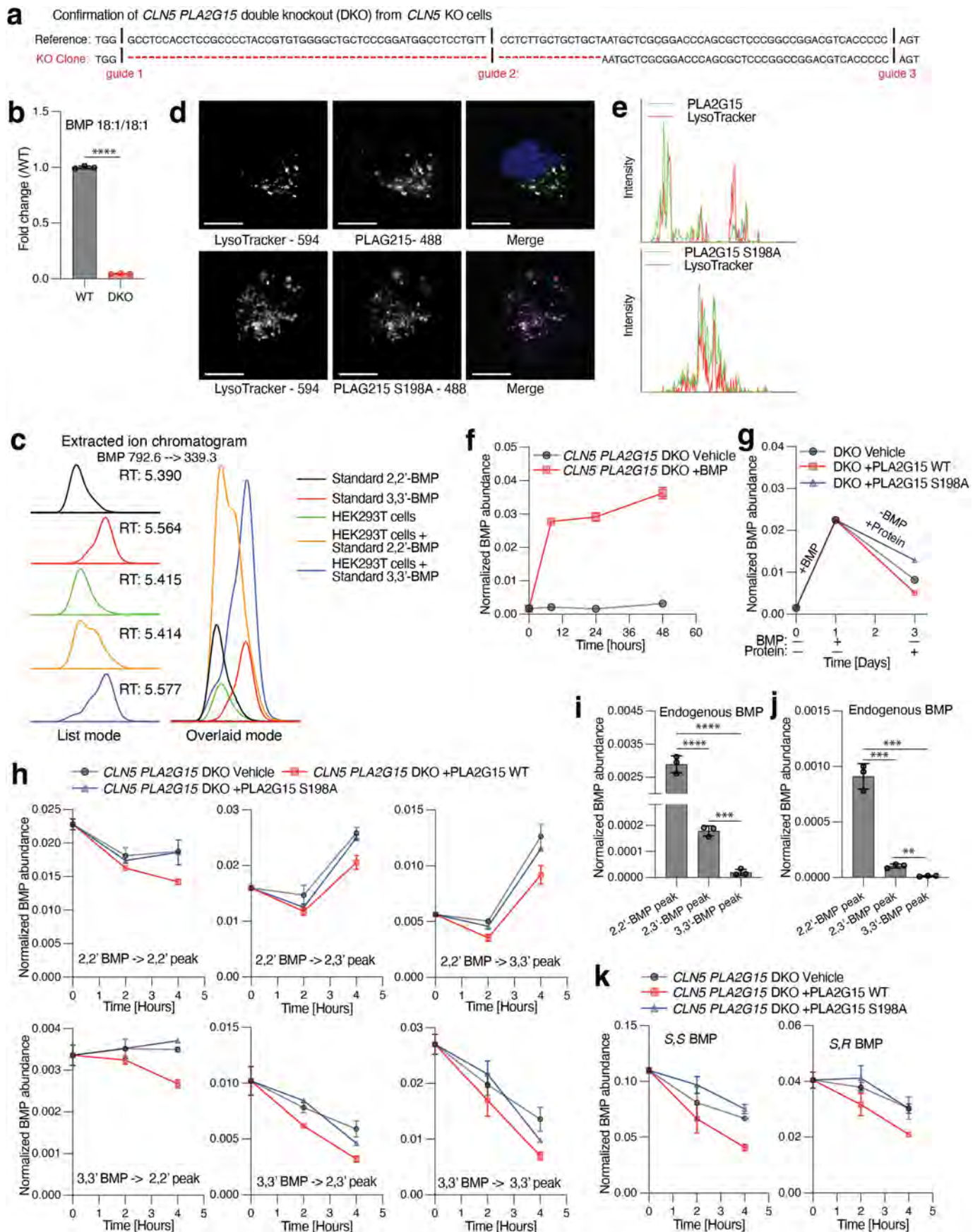
Extended Data Fig. 5 | *sn2, sn2'* esterification position of *S,S* BMP confers resistance to PLA2G15-mediated hydrolysis in vitro. **a**, PLA2G15 efficiently deacylates BMP independent of stereoconfiguration. Hydrolysis of 1 μ M BMP stereoisomers by 100 nM recombinant PLA2G15 for 30 s under acidic conditions (pH=5.0). LPG intermediate was measured with LC-MS. Data are mean \pm s.d. of $n=3$ independent replicates. **b**, A representative image of the extracted ion chromatogram of 2,2' and 3,3' positional BMP isomers used in this paper. Each compound has a minor amount of 2,3' isomer. **c**, LPG monitoring shows minimal difference in the activity of PLA2G15 against positional BMP isomers. Same experiment as in (a) using 1 μ M of either 3,3' *S,S* BMP or 2,2' *S,S* BMP as substrate incubated for 30 secs. Data are mean \pm s.d. of $n=3$ independent replicates. **d,e**, Time course of BMP hydrolysis shows 2,2' BMP positional isomer confers resistance to PLA2G15 degradation. Hydrolysis of 20 μ M 2,2' *S,S* BMP or 3,3' *S,S* BMP positional isomers as well as equimolar amount of both by

100 nM recombinant PLA2G15 over 10 h under acidic conditions (pH=5.0). Controls had similar reaction buffers except with no enzyme. BMP hydrolase activity was determined using LC-MS by measuring the abundance of LPG intermediate in (d) and GPG product in (e). Data are mean \pm s.d. of $n=3$ independent replicates. **f**, DiffDock of 3,3' *S,S* BMP onto AlphaFold human PLA2G15 structure. Catalytic triad residues Ser198, Asp360 and His392 of the active site of PLA2G15 are annotated. **g**, BMP binds to PLA2G15 S198A at low micromolar concentration. Binding affinity was determined using microscale thermophoresis for 3,3' *S,S* BMP. Data presented as mean \pm s.e.m. from three measurements. **h**, Chemical structures of other BMP lipids used in this study. **i**, Time dependent hydrolysis of BMP stereoisomers confirms *S,S* stereochemistry of 2,2' BMP contributes to resistance to PLA2G15-dependent degradation. Assay as in (d) using indicated BMP isomers over 1 hour under acidic conditions (pH=5.0). Data are mean \pm s.d. of $n=3$ independent replicates.

Article

Extended Data Fig. 6 | PLA2G15-deficient cells and lysosomes accumulate BMP. **a,b**, Targeted analyses of BMP lipids in PLA2G15-deficient cells reveal their accumulation in lysosomes and whole cells. **a**, Heatmap representation of log₂-transformed changes in BMP abundances in lysosomes (IP) and whole cells (WC) of PLA2G15-deficient HEK293T clone1 compared to wildtype control ($n = 3$ WT and $n = 3$ PLA2G15 KO). Data are the ratio of the mean of each BMP. Significant changes from the graph are represented by * $p < 0.05$. P values were calculated using two-tailed unpaired t -tests and are presented in Supplementary Table 1. **b**, Fold changes in total BMP abundance. The sum of all abundances of measured BMPs was used to generate these values. Data are mean \pm s.d. Statistical analysis was performed using two-tailed unpaired t -tests. ** $p = 0.0013$, **** $p = 0.000051$. **c**, Generation of PLA2G15-deficient clones 2 and 3. **d**, Schematic for fluorescently labeled PLA2G15 uptake experiments. Labeled recombinant PLA2G15 proteins were supplemented to PLA2G15 KO HEK293T cells for 48 h and imaged to validate delivery. **e**, Representative images of labeled PLA2G15 wildtype and mutant proteins (Alexa488) and lysosomes (Lysotracker) show successful uptake and trafficking in PLA2G15 KO HEK293T cells (left). In the merged images, green and magenta represents the protein and Lysotracker channel respectively and white represents the colocalized spots. Scale bar = 5 μ m. Intensity showing that labeled proteins colocalize with Lysotracker (right). Each experiment was repeated three times. **f**, Recombinant PLA2G15 does not rescue elevated levels of around a fifth of BMPs resulting from PLA2G15 loss. Fold changes in the levels of BMPs in PLA2G15 KO HEK293T cells after supplementation with wildtype or mutant PLA2G15 ($n = 3$ WT, $n = 3$

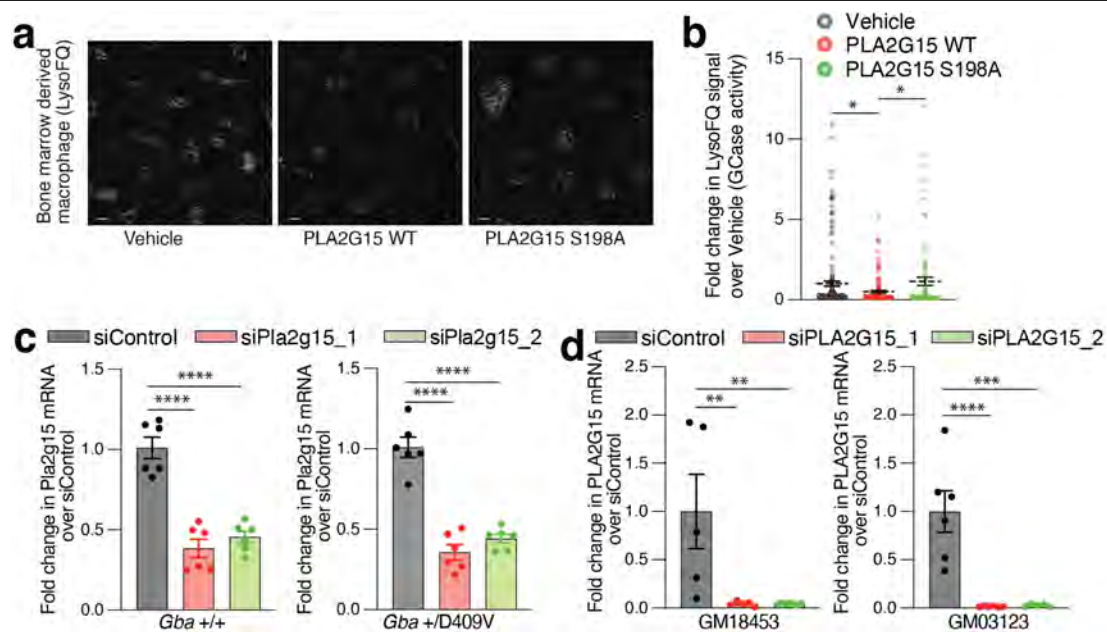
PLA2G15 KO, $n = 3$ PLA2G15 KO + PLA2G15 and $n = 3$ PLA2G15 KO + PLA2G15 S198A). Data are mean \pm s.d. Statistical analysis was performed using two-tailed unpaired t -tests. ** $p = 0.0012$, *** $p < 0.001$ and **** $p < 0.0001$. **g**, Targeted analyses of BMP lipids reveal that a deficiency in PLA2G15 increases levels of most BMPs in HeLa cells. Data are mean \pm s.d. (right) ($n = 3$ WT and $n = 3$ PLA2G15 KO). Statistical analysis was performed using two-tailed unpaired t -tests. * $p < 0.05$, ** $p = 0.0017$, *** $p < 0.001$ and **** $p < 0.0001$. Individual BMP species and their statistics are presented in Supplementary Table 3. **h**, Targeted analyses show minimal phospholipid alterations in PLA2G15-deficient mouse tissues (top), HEK293T cells and lysosomes (bottom). Heatmap representation of log₂-transformed changes in total lipid class in PLA2G15-deficient mouse tissues (mouse brain, kidney and liver) compared to their control counterparts ($n = 6$ WT and $n = 6$ *Pla2g15*^{-/-}) and PLA2G15-deficient HEK293T cells compared to wildtype cells ($n = 3$ PLA2G15 KO and $n = 3$ WT). Data are the ratio of the mean of each lipid class. Significant changes from the graph are represented by * $p < 0.05$. P values were calculated using two-tailed unpaired t -tests. All measured individual lipid species, total lipid classes and their statistics are presented in Supplementary Table 5. **i,j**, Loss of PLA2G15 has no effect on BMP synthesis and lysosomal biogenesis. **i**, Immunoblot analysis of lysosomal markers (LAMP2 and Cathepsin B), the BMP synthase CLN5 and a loading control (Vinculin). **j**, BMP synthesis in HEK293T cells using labeled phosphatidylglycerol (D5-PG) at the indicated time points. $n = 3$ WT and $n = 3$ PLA2G15 KO. Data are mean \pm s.d. Gel source data are provided in Supplementary Fig. 1. Panel **d** was created using BioRender (<https://biorender.com>).



Extended Data Fig. 7 | See next page for caption.

Extended Data Fig. 7 | Esterification position in BMP confers resistance to hydrolysis in cells. **a**, Generation and sequence validation of *PLA2G15* KO on a background of *CLN5* KO HEK293T cells (DKO). **b**, BMP signal is diminished in *CLN5* *PLA2G15* double KO HEK293T cells compared to wildtype. Fold changes of normalized BMP 18:1/18:1 abundance. Data are mean \pm s.d. Statistical analysis was performed using two-tailed unpaired *t*-tests. *****p* = 1.72×10^{-8} . **c**, Supplementation of synthesized positional isomers to HEK293T cells demonstrates 2,2' BMP as the major BMP form in cells. Representative smoothened graphs of the extracted ion chromatograms following addition of 2,2' and 3,3' BMP standards to *CLN5* *PLA2G15* double KO HEK293T cells. The retention times are shown in the list mode (left) while the alignment of standards in overlaid mode (right) indicate 2,2' BMP as the predominant endogenous form. **d**, Representative images of labeled *PLA2G15* wildtype and mutant proteins (Alexa488) and lysosomes (LysoTracker) show successful uptake and trafficking in *CLN5* *PLA2G15* KO HEK293T cells. In the merged images, green and magenta represents the protein and LysoTracker channel respectively and white represents the colocalized spots. Scale bar = 5 μ m. Each experiment was repeated three times. **e**, Curve represents intensity showing that labeled proteins (green) colocalizes with LysoTracker (red) as marker for the lysosome. **f**, Exogenous BMP feeding to cells was optimized for pulse-chase experiments. Normalized BMP abundance was measured following addition of 3,3' BMP at indicated time points. Data are mean \pm s.d. of *n* = 3 independent replicates. **g**, *PLA2G15* WT hydrolyzes BMP in cells while cells supplemented with inactive *PLA2G15* S198A exhibit reduced BMP hydrolysis capacity. 100 nM *PLA2G15* proteins were supplemented in the chase period after delivery of 10 μ M 2,2' *S,S* BMP for two hours. **h-j**, Turnover of 3,3' *S,S* BMP is rapid while 2,2' BMP may require positional isomerization for efficient degradation in cells. **h**, The intensity of each BMP peak (2,2' BMP peak; left, 2,3' BMP peak; middle, 3,3' BMP peak; right) was quantified following a 4-hour chase by *PLA2G15* proteins or no enzyme control following addition of either 10 μ M of 2,2' *S,S* BMP (top) or 3,3' *S,S* BMP (bottom). *PLA2G15* quickly hydrolyzes 3,3' and 2,3' BMP after 3,3' BMP supplementation while 2,2' BMP is converted to 2,3' and 3,3' BMP. Data are mean \pm s.d. of *n* = 3 independent replicates. **i**, Quantitation of endogenous BMP peaks during pulse-chase experiment in cells that were not supplemented with BMP in (h). These levels are minimal compared to cells supplemented with the lipids. Data are mean \pm s.d. of *n* = 3 independent replicates. Statistical analysis was performed using two-tailed unpaired *t*-tests. ****p* = 0.0003 and *****p* < 0.0001. **j**, Quantitation of endogenous BMP peaks in cells that were not supplemented with BMP during pulse-chase experiment (Fig. 4d-f) using equimolar mixture of 2,2' BMP and 3,3' BMP. Data are mean \pm s.d. of *n* = 3 independent replicates. Statistical analysis was performed using two-tailed unpaired *t*-tests. ***p* = 0.0011 and ****p* < 0.001. **k**, BMP stereoisomers are degraded similarly in cells. Same experiment as in (h) using *S,S* BMP (left) and *S,R* BMP (right) to measure total BMP levels during chase. Data are mean \pm s.d. of *n* = 3 independent replicates.

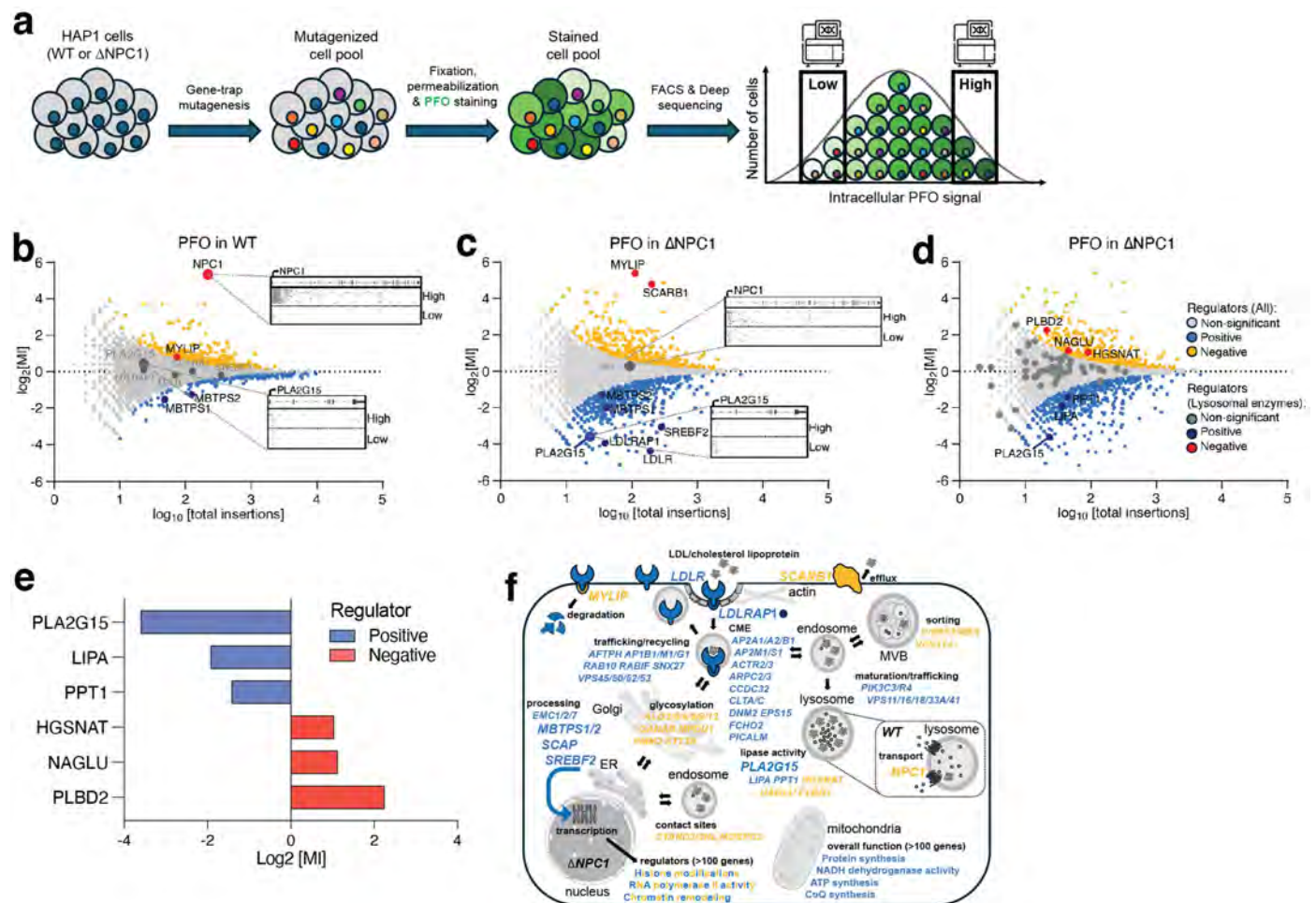
replicates. **g**, *PLA2G15* WT hydrolyzes BMP in cells while cells supplemented with inactive *PLA2G15* S198A exhibit reduced BMP hydrolysis capacity. 100 nM *PLA2G15* proteins were supplemented in the chase period after delivery of 10 μ M 2,2' *S,S* BMP for two hours. **h-j**, Turnover of 3,3' *S,S* BMP is rapid while 2,2' BMP may require positional isomerization for efficient degradation in cells. **h**, The intensity of each BMP peak (2,2' BMP peak; left, 2,3' BMP peak; middle, 3,3' BMP peak; right) was quantified following a 4-hour chase by *PLA2G15* proteins or no enzyme control following addition of either 10 μ M of 2,2' *S,S* BMP (top) or 3,3' *S,S* BMP (bottom). *PLA2G15* quickly hydrolyzes 3,3' and 2,3' BMP after 3,3' BMP supplementation while 2,2' BMP is converted to 2,3' and 3,3' BMP. Data are mean \pm s.d. of *n* = 3 independent replicates. **i**, Quantitation of endogenous BMP peaks during pulse-chase experiment in cells that were not supplemented with BMP in (h). These levels are minimal compared to cells supplemented with the lipids. Data are mean \pm s.d. of *n* = 3 independent replicates. Statistical analysis was performed using two-tailed unpaired *t*-tests. ****p* = 0.0003 and *****p* < 0.0001. **j**, Quantitation of endogenous BMP peaks in cells that were not supplemented with BMP during pulse-chase experiment (Fig. 4d-f) using equimolar mixture of 2,2' BMP and 3,3' BMP. Data are mean \pm s.d. of *n* = 3 independent replicates. Statistical analysis was performed using two-tailed unpaired *t*-tests. ***p* = 0.0011 and ****p* < 0.001. **k**, BMP stereoisomers are degraded similarly in cells. Same experiment as in (h) using *S,S* BMP (left) and *S,R* BMP (right) to measure total BMP levels during chase. Data are mean \pm s.d. of *n* = 3 independent replicates.



Extended Data Fig. 8 | PLA2G15 role in lysosomal lipid metabolism.

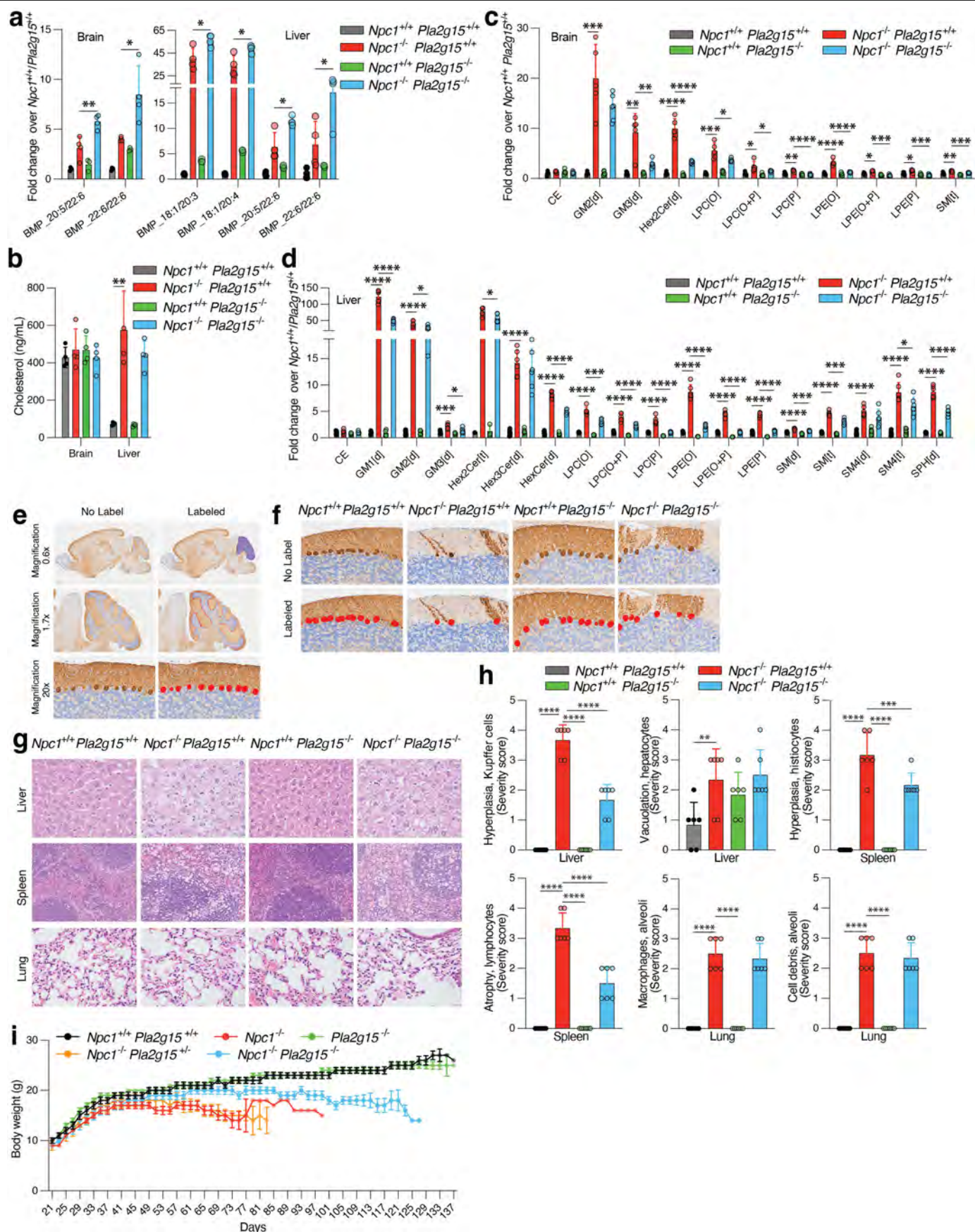
a,b, PLA2G15 supplementation reduces GCase activity in bone marrow derived macrophages (BMDMs). **a**, Representative fluorescence microscopy images of BMDMs treated with 300 nM recombinant PLA2G15 WT, inactive PLA2G15 S198A or vehicle buffer (PBS) overnight followed by a 30-min incubation of 10 μ M LysoFQ-GBA to measure GCase activity. **b**, Quantification of signal intensity of LysoFQ-GBA. Signals were normalized to vehicle treated BMDMs. Data are mean \pm s.e.m. (Vehicle $n = 194$ fields, PLA2G15 WT $n = 118$ and PLA2G15 S198A $n = 83$ of cells). * $p < 0.05$, by one-way ANOVA Fisher's LSD test. **c**, Pla2g15 knockdown in wildtype and mutant *Gba* mouse-derived BMDMs after two-day treatment with 10 nM control siRNA or two different siRNA that target Pla2g15.

qPCR quantification of Pla2g15 mRNA abundance relative to siControl. Actin was used as endogenous control. Data are mean \pm s.e.m. ($n = 6$ per condition). **** $p < 0.0001$, by one-way ANOVA Fisher's LSD test. **d**, PLA2G15 knockdown in two independent NPC1 patient fibroblast cell lines (Coriell GM03123 and GM18453) after two-day treatment with 10 nM control siRNA or two different siRNA that target PLA2G15. qPCR quantification of PLA2G15 mRNA abundance relative to siControl. GAPDH was used as endogenous control. Data are mean \pm s.e.m. For GM18453 (siControl $n = 5$, siPLA2G15_1 $n = 5$ and siPLA2G15_2 $n = 6$) and for GM03123 (siControl $n = 6$, siPLA2G15_1 $n = 6$ and siPLA2G15_2 $n = 5$). **** $p < 0.0001$, by one-way ANOVA Fisher's LSD test.



Extended Data Fig. 9 | Haploid genetic screens for genes affecting intracellular cholesterol staining. **a**, Schematic overview of the haploid genetic screens in Hap1 cells. Mutagenized cell libraries were stained for intracellular cholesterol staining using fluorescently labeled PFO. Subsequently, cells are sorted by flow cytometry to obtain cell populations with high and low levels of PFO signal. PFO-HIGH versus PFO-LOW represent the 5% of cells with the highest and lowest fluorescent signal, respectively. **b, c**, Fishtail plots depicting genetic modifiers of intracellular cholesterol in screens of wild-type (**b**) and NPC1-deficient (**c**) Hap1 cells. Insertion sites were mapped in each individual population of cells (i.e. PFO-HIGH versus PFO-LOW) and the log mutational index (MI; see Methods) was plotted against the number of trapped alleles per gene. Statistically significant ($p < 0.05$) positive (whose loss decreases PFO stain) and negative (whose loss increases PFO stain) regulators are coloured blue and orange, respectively. The screen in wild-type Hap1 cells (**b**) identified NPC1 as a strong negative regulator of cholesterol staining as expected (in red). In contrast, the screen in NPC1-deficient cells (**c**) identified genes associated with cholesterol uptake and efflux as strong regulators (i.e. MYLIP, LDLR, LDLRAP1, SREBF2, SCAP, MBTPS1, MBTPS2, SCARB1). In addition, PLA2G15 was identified as a genetic modifier of cholesterol staining (in blue). Note that PLA2G15 was not identified to affect the phenotype in wildtype Hap1 cells. Individual gene-trap insertions (dark grey dots) and their distribution across the gene bodies in PFO-HIGH and PFO-LOW channels of both screens are shown

for NPC1 and PLA2G15. **d**, Same as **c** but lysosomal genes are highlighted. Out of 55 lysosomal enzyme-encoding genes, 6 appear to regulate cholesterol staining in NPC1-deficient cells. The non-significant genes are labeled dark grey ($n = 49$), while the positive ($n = 3$) and negative ($n = 3$) regulators are labeled in dark blue and red, respectively. **e**, Of the 6 identified lysosomal enzyme genes, PLA2G15 appears to be the strongest positive regulator of the cholesterol staining in NPC1-deficient cells. The other genes include LIPA (Lipase A, lysosomal acid type), PPT1 (Palmitoyl-protein thioesterase 1), NAGLU (N-acetyl-alpha-glucosaminidase), HGSNAT (Heparan-alpha-glucosaminide N-acetyltransferase), and PLBD2 (Phospholipase B Domain Containing 2). The list of 55 enzyme genes can be found in Supplementary Table 6 together with all other screen data. **f**, Visualization of top hits with known functions in cellular pathways according to GeneCards. Positive and negative regulators are coloured blue and orange, consistent with the fishtail plots in **b** and **c**. Positive regulators (in blue) include genes affecting clathrin-mediated endocytosis (CME), receptor trafficking/recycling, endosome maturation/trafficking, and mitochondrial function. Negative regulators (in orange) include genes affecting glycosylation, organelle contact sites, and cargo sorting. Key regulators are indicated with larger font size. Icons in **a** adapted from Flaticon (<https://www.flaticon.com/>). Images in **e** adapted from Servier Medical Art (<https://smart.servier.com/>) under a Creative Commons Licence CC BY 4.0.



Extended Data Fig. 10 | See next page for caption.

Extended Data Fig. 10 | Genetic targeting of *Pla2g15* ameliorates defects in NPC1-deficient mouse. **a**, PLA2G15 depletion increases levels of only few BMPs in NPC1-deficient mice. Fold changes in the levels of selected BMPs measured on the QQQ mass spectrometer in all genotypes over *Npc1^{+/+} Pla2g15^{+/+}* brain (left) and liver (right). Data are mean \pm s.d. ($n = 4$, for all genotypes except $n = 3$ for *Npc1^{+/+} Pla2g15^{-/-}*). Statistical analysis was performed using two-tailed unpaired *t*-tests. * $p < 0.05$ and ** $p = 0.0072$. All measured BMP species and their statistics are presented in Supplementary Table 7. **b**, Cholesterol staining. Cholesterol was measured in left hemibrain and left liver lobe ($n = 4$ per group). Data are mean \pm s.d. Statistical analysis was performed using one-way ANOVA followed by Bonferroni's multiple comparisons. ** $p = 0.00295$. **c, d**, Genetic depletion of PLA2G15 reverses secondary lipid storage in NPC1-deficient brain (c) and liver (d) mouse tissues. Fold changes in the levels of selected total lipid classes in all genotypes compared to *Npc1^{+/+} Pla2g15^{+/+}* brain (c) and liver (d). Data are mean \pm s.d. ($n = 5$, for all brain genotypes except $n = 6$ for brain *Npc1^{-/-} Pla2g15^{-/-}* and $n = 6$, for all liver genotypes). Statistical analysis was performed using two-tailed unpaired *t*-tests. * $p < 0.05$, ** $p < 0.01$, *** $p < 0.001$,

**** $p < 0.0001$. All measured individual lipid species, total lipid classes and their statistics are presented in Supplementary Table 8. **e, f**, Purkinje cell count by histomorphometry on Calbindin-immunolabelled CNS sections. **e**, Proof-of-concept of the image analysis indicating the annotations in the cerebellum (ROI: Region of Interest) and the detection of Purkinje cell soma at different magnifications. **f**, Representative images of the cerebellum at the level of lobe II/III for comparison among study groups. No label: Scanned whole slide images (WSI) prior to image analysis. Labeled: WSI indicating the annotations of the ROI and the detections of Purkinje cell's soma. **g, h**, Genetic ablation of PLA2G15 decreases histopathology lesions in NPC1-deficient mice. The microscopy images are in g and their mean severity scores of each histopathology finding are shown in h. Data are mean \pm s.d of $n = 6$ independent replicates. ** $p = 0.0063$, *** $p = 0.0006$ and **** $p < 0.0001$, by one-way ANOVA Fisher's LSD test comparing NPC1-deficient tissues to other genotypes. Scale bar is 20 μm . **i**, Body weight assessment for all genotypes. Animal body weight was measured every other day starting at 3 weeks old. Data are mean \pm s.e.m. of $n = 12$, 6 males and 6 females per genotype.

Reporting Summary

Nature Portfolio wishes to improve the reproducibility of the work that we publish. This form provides structure for consistency and transparency in reporting. For further information on Nature Portfolio policies, see our [Editorial Policies](#) and the [Editorial Policy Checklist](#).

Statistics

For all statistical analyses, confirm that the following items are present in the figure legend, table legend, main text, or Methods section.

n/a	Confirmed
<input type="checkbox"/>	<input checked="" type="checkbox"/> The exact sample size (n) for each experimental group/condition, given as a discrete number and unit of measurement
<input type="checkbox"/>	<input checked="" type="checkbox"/> A statement on whether measurements were taken from distinct samples or whether the same sample was measured repeatedly
<input type="checkbox"/>	<input checked="" type="checkbox"/> The statistical test(s) used AND whether they are one- or two-sided <i>Only common tests should be described solely by name; describe more complex techniques in the Methods section.</i>
<input checked="" type="checkbox"/>	<input type="checkbox"/> A description of all covariates tested
<input checked="" type="checkbox"/>	<input type="checkbox"/> A description of any assumptions or corrections, such as tests of normality and adjustment for multiple comparisons
<input type="checkbox"/>	<input checked="" type="checkbox"/> A full description of the statistical parameters including central tendency (e.g. means) or other basic estimates (e.g. regression coefficient) AND variation (e.g. standard deviation) or associated estimates of uncertainty (e.g. confidence intervals)
<input type="checkbox"/>	<input checked="" type="checkbox"/> For null hypothesis testing, the test statistic (e.g. F , t , r) with confidence intervals, effect sizes, degrees of freedom and P value noted <i>Give P values as exact values whenever suitable.</i>
<input checked="" type="checkbox"/>	<input type="checkbox"/> For Bayesian analysis, information on the choice of priors and Markov chain Monte Carlo settings
<input checked="" type="checkbox"/>	<input type="checkbox"/> For hierarchical and complex designs, identification of the appropriate level for tests and full reporting of outcomes
<input checked="" type="checkbox"/>	<input type="checkbox"/> Estimates of effect sizes (e.g. Cohen's d , Pearson's r), indicating how they were calculated

Our web collection on [statistics for biologists](#) contains articles on many of the points above.

Software and code

Policy information about [availability of computer code](#)

Data collection	All softwares for data collection are publicly or commercially available: Agilent QQQ, Lecia LSM980 ZEN microscopy software Zen3.6 (blue edition), Olympus microscope BX46, Leica Biosystems Bond VIII, Thermo Scientific Orbitrap mass spectrometer v3.3.2782.34
Data analysis	All softwares for data analysis are publicly or commercially available: Microsoft Excel v16.72, Agilent quantitative software v10.0, ImageJ v2.1.0, Cellprofiler v4.7.2, QuPath v0.4.3 and GraphPad Prism v10.0.

For manuscripts utilizing custom algorithms or software that are central to the research but not yet described in published literature, software must be made available to editors and reviewers. We strongly encourage code deposition in a community repository (e.g. GitHub). See the Nature Portfolio [guidelines for submitting code & software](#) for further information.

Data

Policy information about [availability of data](#)

All manuscripts must include a [data availability statement](#). This statement should provide the following information, where applicable:

- Accession codes, unique identifiers, or web links for publicly available datasets
- A description of any restrictions on data availability
- For clinical datasets or third party data, please ensure that the statement adheres to our [policy](#)

All data needed to evaluate the conclusions stated in the paper are present in the paper and/or the Supplementary Materials. This paper does not report original code. Cell lines can be requested, and requests will be fulfilled by, the lead author, Monther Abu-Remaileh (monther@stanford.edu). All sequencing datasets from

the haploid screens have been deposited in the NCBI Sequence Read Archive under accession number PRJNA1177366. Data from untargeted lipid profiling are deposited at Zenodo under accession number 14170856.

Research involving human participants, their data, or biological material

Policy information about studies with [human participants or human data](#). See also policy information about [sex, gender \(identity/presentation\), and sexual orientation](#) and [race, ethnicity and racism](#).

Reporting on sex and gender Not applicable

Reporting on race, ethnicity, or other socially relevant groupings Not applicable

Population characteristics Not applicable

Recruitment Not applicable

Ethics oversight Not applicable

Note that full information on the approval of the study protocol must also be provided in the manuscript.

Field-specific reporting

Please select the one below that is the best fit for your research. If you are not sure, read the appropriate sections before making your selection.

☒ Life sciences ☐ Behavioural & social sciences ☐ Ecological, evolutionary & environmental sciences

For a reference copy of the document with all sections, see nature.com/documents/nr-reporting-summary-flat.pdf

Life sciences study design

All studies must disclose on these points even when the disclosure is negative.

Sample size Based on previously published work (<https://pubmed.ncbi.nlm.nih.gov/36131016/>), we used a minimum of size of $n = 3$ for quantitative experiments. For in vivo experiments, the final numbers were determined based on availability of each genotype, experimental design and animal housing conditions and we observed that sample sizes of 5 to 12 animals were adequate to obtain statistical power. For cell based experiments, each independent culture of cells was defined as biological replicate.

Data exclusions In rare cases where we had poor detection across majority of the lipids, the whole sample was excluded.

Replication For most of our figures, at least three independent experiments were performed and have not encountered discrepancy in results and conclusions

Randomization For targeted mass spectrometry acquisition, samples were often randomized to prevent any systematic bias and column carry over. For pairwise comparisons, samples were processed in internally controlled pairs (i.e Wild type vs KO), while matching age and sex. For other experiments where samples were not allocated randomly, group allocation and randomization were unnecessary because all samples were measured independently in the same way in an internally controlled manner

Blinding Sample blinding was not performed for most experiments as they did not involve formal qualitative scoring. Furthermore, all measurement modalities were quantitative and all samples in all experiments were performed in the same way regardless of group or treatment. Immunofluorescence (IF) assessments were qualitative and based on identifiable features. In at least one replicate for each IF experiment, samples were independently evaluated by one other investigator whose interpretation supported the conclusions in the manuscript.

Reporting for specific materials, systems and methods

We require information from authors about some types of materials, experimental systems and methods used in many studies. Here, indicate whether each material, system or method listed is relevant to your study. If you are not sure if a list item applies to your research, read the appropriate section before selecting a response.

Materials & experimental systems

n/a	Involved in the study
<input type="checkbox"/>	<input checked="" type="checkbox"/> Antibodies
<input type="checkbox"/>	<input checked="" type="checkbox"/> Eukaryotic cell lines
<input checked="" type="checkbox"/>	<input type="checkbox"/> Palaeontology and archaeology
<input type="checkbox"/>	<input checked="" type="checkbox"/> Animals and other organisms
<input checked="" type="checkbox"/>	<input type="checkbox"/> Clinical data
<input checked="" type="checkbox"/>	<input type="checkbox"/> Dual use research of concern
<input checked="" type="checkbox"/>	<input type="checkbox"/> Plants

Methods

n/a	Involved in the study
<input checked="" type="checkbox"/>	<input type="checkbox"/> ChIP-seq
<input checked="" type="checkbox"/>	<input type="checkbox"/> Flow cytometry
<input checked="" type="checkbox"/>	<input type="checkbox"/> MRI-based neuroimaging

Antibodies

Antibodies used

His: CST 2365, Mouse HRP: CST 7076, Rabbit HRP: CST 7074, LAMP2; SC-18822, Vinculin: SC-73614, CTSB: CST-31718, CLN5: Ab170899, GFAP: Ab7260, Calbindin: Ab229915, MBP: Ab218011, Iba1: Ab178846. All CST are from Cell Signaling Technology, SC from Santa Cruz Biotechnology) and Ab from Abcam.

Validation

All antibodies used in this study are acquired from commercial sources and were validated for specificity and species reactivity by the manufacturer. The information is readily available on the website of the manufacturer through the above-mentioned cat#. and listed below

https://www.cellsignal.com/products/primary-antibodies/his-tag-antibody/2365/
 https://www.cellsignal.com/products/secondary-antibodies/anti-mouse-igg-hrp-linked-antibody/7076
 https://www.cellsignal.com/products/secondary-antibodies/anti-rabbit-igg-hrp-linked-antibody/7074
 https://www.scbt.com/p/lamp-2-antibody-h4b4
 https://www.scbt.com/p/vinculin-antibody-7f9
 https://www.cellsignal.com/products/primary-antibodies/cathepsin-b-d1c7y-xp-rabbit-mab/31718
 https://www.abcam.com/en-us/products/primary-antibodies/cln5-antibody-epr12197b-ab170899
 https://www.abcam.com/en-us/products/primary-antibodies/gfap-antibody-ab7260
 https://www.abcam.com/en-us/products/primary-antibodies/calbindin-antibody-epr22698-236-ab229915
 https://www.abcam.com/en-us/products/primary-antibodies/myelin-basic-protein-antibody-epr21188-ab218011
 https://www.abcam.com/en-us/products/primary-antibodies/iba1-antibody-epr16588-ab178846

Eukaryotic cell lines

Policy information about [cell lines and Sex and Gender in Research](#)

Cell line source(s)

HEK 293T and HeLa cells were from ATCC. Expi 293F cells (Thermo Fisher Scientific A14527) were a gift from Peter Kim at Stanford University. HAP1 cells were acquired under license with the Whitehead Institute and the Netherlands Cancer Institute.

Authentication

STR profiling and genetic analysis

Mycoplasma contamination

Test routinely and negative results obtained

Commonly misidentified lines
(See [ICLAC](#) register)

No commonly misidentified cell lines were used in this study

Animals and other research organisms

Policy information about [studies involving animals; ARRIVE guidelines](#) recommended for reporting animal research, and [Sex and Gender in Research](#)

Laboratory animals

Experiments were performed in the following mouse strains: Lysotag mice, Npc1+/+ Pla2g15-/-, Npc1-/- Pla2g15+/-, Npc1-/- Pla2g15-/-, Npc1-/- Pla2g15+/-, Gba D409V and wild type mice. All mice had an average age of 2 months and were maintained on a standard light-dark cycle with access to food and water. Cages were cleaned regularly and supplies of water and food were checked daily

Wild animals

None

Reporting on sex

Sex of mice are indicated in the figure legends and/or supplementary tables for each experiment.

Field-collected samples	None
Ethics oversight	All procedures involving mice were carried out in accordance with the approved guidelines by Stanford University, University of Wisconsin and Animal Care and Welfare committee in Austria

Note that full information on the approval of the study protocol must also be provided in the manuscript.

Plants

Seed stocks	Not applicable
Novel plant genotypes	Not applicable
Authentication	Not applicable